

Supporting Information For: Electrolyte Immersion Increases Photoconductivity in a Model Polymer Photocathode

William P. Kopcha,^{†,‡} Aiswarya Abhisek Mohapatra,^{†,¶} Casey M. Davis,[§]
Jonathan R. Thurston,[§] Eui Hyun Suh,^{||} Bo Dong,[⊥] Megan R. Brown,[#]
Aniruddha Basu,[¶] Zejie Chen,[@] Shane Ardo,^{@,△,∇} Chad M. Risko,[#] Tianquan
Lian,[⊥] Erin L. Ratcliff,^{||} Stephen Barlow,^{¶,‡} Seth R. Marder,^{¶,§,††,‡‡,‡} Michael F.
Toney,^{¶,††,‡‡} Melissa K. Gish,^{*,‡} Andrew J. Ferguson,^{*,‡} and Obadiah G. Reid^{*,‡,¶}

[†]*These authors contributed equally to this work.*

[‡]*Materials, Chemical, and Computational Science Directorate, National Renewable Energy Laboratory.
Golden CO 80401, USA*

[¶]*Renewable and Sustainable Energy Institute, University of Colorado Boulder. Boulder CO 80309, USA*

[§]*Department of Chemistry, University of Colorado Boulder. Boulder CO 80309, USA*

^{||}*School of Materials Science and Engineering, Georgia Institute of Technology. Atlanta GA 30332, USA*

[⊥]*Department of Chemistry, Emory University. Atlanta GA, USA 30322*

[#]*Department of Chemistry, University of Kentucky. Lexington, KY USA 40506*

[@]*Department of Chemistry, University of California Irvine. Irvine CA, USA 92697*

[△]*Department of Chemical and Biomolecular Engineering*

[∇]*Department of Materials Science and Engineering*

^{††}*Department of Chemical and Biological Engineering, University of Colorado Boulder. Boulder CO 80309,
USA*

^{‡‡}*Materials Science and Engineering Program, University of Colorado Boulder. Boulder CO 80309, USA*

E-mail: melissa.gish@nrel.gov; andrew.ferguson@nrel.gov; obadiah.reid@colorado.edu

Contents

1	Experimental Details	3
1.1	Sources for Chemicals and Reagents	3
1.2	Film Preparation for Spectroscopic Experiments	4
1.3	Photocathode Preparation	4
1.4	UV-Vis-NIR Absorbance	5
1.5	Photoluminescence (PL)	5
1.6	FTIR	6
1.7	Time Resolved Microwave Conductivity (TRMC)	6
1.8	Steady State Microwave Conductivity (SSMC)	11
1.9	Transient Absorption	12
1.10	Sample Prep for TA	13
1.11	Steady State PhotoInduced Absorption (SSPIA)	13
1.12	X-Ray Reflectivity (XRR)	15
1.13	Grazing-Incidence Wide-Angle X-ray Scattering (GIWAXS)	17
1.14	Computational Methods	18
2	Addressing Potential Confounding Variables	19
2.1	Pd Removal Procedure	19
2.2	Photophysical Properties of Treated vs. Untreated Films	20
2.3	The Impact of Dissolved Oxygen	21
3	Supplementary Data for Main Text	22
3.1	Profilometry	22
3.2	Absorbance	22
3.3	Detection of Absorbed Water by FTIR	24
3.4	Hydrogen Evolution Experiments	25
3.5	Stability Testing	26

3.6	SSMC Frequency Scans	28
3.7	TRMC Transients	29
3.8	Additional Discussion of the Dielectric Impact of Water	31
3.9	Additional Discussion of SSPIA Experiments	35
3.10	Additional Discussion of the 1300 nm Photoinduced Absorption Feature in TA	38
3.11	Computational Spectral Determination	41
3.12	Triplet Sensitization Experiments	44
3.13	Additional Discussion of TA Data	45
3.14	The Impact of Pt Nanoparticles on Charge Dynamics	60
	References	62

1 Experimental Details

1.1 Sources for Chemicals and Reagents

5,10,15,20-Tetraphenyl-21H,23H-porphine iron(III) chloride (TPPIC), polystyrene (PS), sodium sulfate, sodium chloride, sulfuric acid were purchased from Sigma-Aldrich and used without further purification. Poly(4,8-bis(5-(2-ethylhexyl)thiophen-2-yl)benzo [1,2-*b*:4,5-*b'*]dithiophene-2,6-diyl)-*alt*-(2-(((2-ethylhexyl)oxy)carbonyl)-3-fluorothieno [3,4-*b*]thiophene-4,6-diyl) (PTB7-Th) and poly(*N,N'*-di(2-octyldodecyl)naphthalene-1,8:4,5-bis(dicarboximide)-2,6-diyl)-*alt*-(2,2-bithiophene-5,5'-diyl) (N2200) were purchased from 1-materials and used after purifying of palladium residues following a literature reported procedure.¹ [2-(3,6-Dimethyl-9H-carbazol-9-yl)ethyl]phosphonic acid (Me-2PACz) was purchased from TCI. Absolute ethanol was purchased from Thermo Fisher. K₂PtCl₄ was purchased from Sigma-Aldrich. lead(II) tetrakis(4-cumylphenoxy)phthalocyanine (PbPc) and free-base tetraphenyl porphyrin were purchased from Sigma-Aldrich and used as received.

1.2 Film Preparation for Spectroscopic Experiments

Films were made by mixing the appropriate polymers in ortho-dichlorobenzene (oDCB) at a total polymer concentration of 15 mg/mL for pure N2200 and PTB7-Th or 16 mg/mL of a 2:1 weight-ratio mixture of the two. These were heated to 80 °C with stirring in the glovebox overnight, followed by spin-coating on 2.2 cm x 1 cm quartz substrates. These had previously been cleaned by sonicating for 10 minutes each in a soap solution, DI water, acetone, and isopropanol, drying under a stream of N₂, and 10 minutes of UV-ozone treatment. A speed of 1400 rpm for 60 seconds with a 500 rpm/s ramp was used for the pure polymers and 2000 rpm for 60 seconds with a 1000 rpm/s ramp for the blend. They were then annealed on a hot plate at 100° for 10 minutes.

1.3 Photocathode Preparation

For photocathodes, ITO substrates (1.5 × 1.5 cm²) were sequentially bath-sonicated in DI water with 1 vol% Triton X-100, acetone, and isopropyl alcohol for 20 min each. Sonicated ITO substrates were additionally UV-ozone cleaned for 20 min. Me-2PACz was dissolved in absolute ethanol (2 mM). 100 μL of Me-2PACz solution was spin-coated on the cleaned ITO substrates at 3000 rpm for 30 s. Me-2PACz-coated ITO substrates were annealed at 100 °C for 10 min and rinsed by dynamic spin coating at 6000 rpm. 50 μL of ethanol was dropped on the films two times on the substrates during spin coating. PTB7-Th and N2200 were dissolved in chlorobenzene (PTB7-Th:N2200 = 2:1 wt/wt; 8 mg mL⁻¹) at 70 °C and stirred at 800 rpm overnight. The blend solution was spin-coated on Me-2PACz-treated ITO substrates at 2000 rpm for 60 s. The films were annealed at 100 °C for 10 min. Pt co-catalysts were electrodeposited on polymer blend layers in a three-electrode system under white LED light irradiation (MWWHL3, Thorlabs, intensity ~100 mW cm⁻²). ITO/Me-2PACz/BHJ, Ag/AgCl/sat. KCl/0.5 M Na₂SO₄ (double junction), and IrO_x-Ta₂O_x-coated Ti plate were used as a working, reference, and counter electrodes, respectively. 0.5 mM K₂PtCl₄ + 0.5 M Na₂SO₄ solution in DI water was used as an electrolyte. The electrolyte was Ar-sparged at

least 30 min before use. 0.1 V (vs. Ag/AgCl) was applied to the working electrode during Pt deposition with an active area of 0.672 cm^2 using a CH instruments 920D bipotentiostat. The estimated Pt loading is 15 mC cm^{-2} , calculated by integrated area of J-t curves during chronoamperometry.

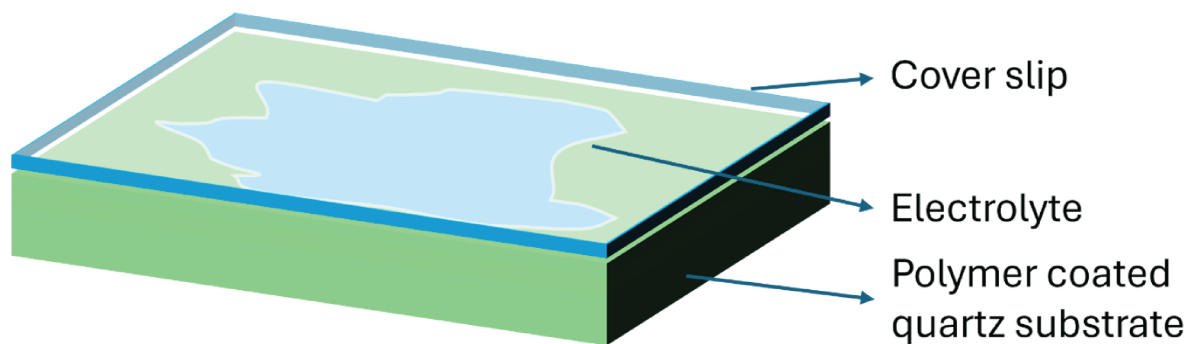


Figure S1: Schematic showing the sample preparation for in situ experiments. To prevent water evaporation, the cover slip was affixed to the substrate using vacuum grease at the edges.

1.4 UV-Vis-NIR Absorbance

UV-visible spectra of the polymer films were collected in transmission mode using a Cary 7000 spectrometer.

1.5 Photoluminescence (PL)

Photoluminescence spectra were recorded using a Princeton PL system equipped with an Energetiq EQ99x laser-driven light source illuminating the sample through a dual (Princeton Instruments HRS-500) monochromators. The emission spectrometer consists of a Princeton Instruments HRS-300 (150 g/mm, 800 nm blaze) coupled to either a vis-NIR (PyLoN 100F) or SWIR (PyLoN IR) liquid nitrogen cooled CCD array. The spectral intensity is calibrated using either a VIS-NIR or SWIR quartz-tungsten halogen lamps provided by Princeton Instruments with in-firmware calibration files.

1.6 FTIR

Fourier-Transform IR measurements were taken using a Nicolet iS50R by Thermo Scientific. Polymer blends were spin-coated onto a CaF_2 window using the same procedure as described for the samples on quartz (*vide supra*). A resolution of 4 cm^{-1} was used. 120 background scans and 120 spectrum scans were taken.

1.7 Time Resolved Microwave Conductivity (TRMC)

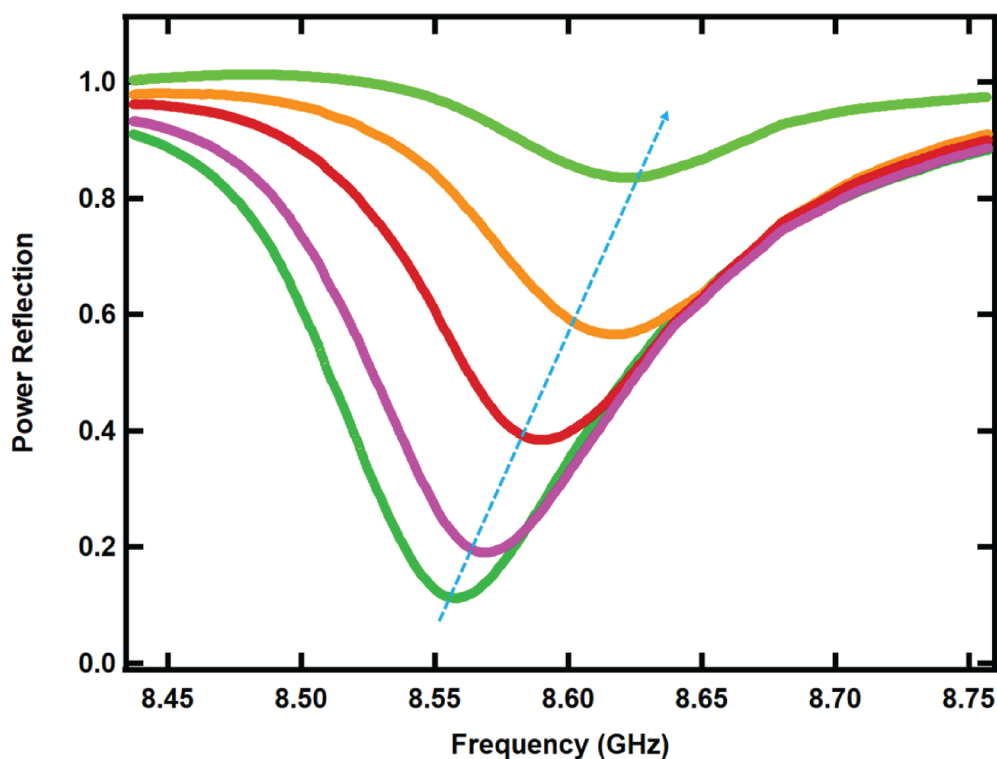


Figure S2: Change in microwave cavity resonance frequency of the PTB7-Th:N2200 (2:1) with gradual loss of water as depicted by the direction of arrow.

In-situ time-resolved microwave conductivity (TRMC) experiments were conducted using DI water, and different concentrations of electrolytes placed on the polymer coated quartz substrates encapsulated using a glass cover slip with vacuum grease at the edges to prevent water loss during the measurement (Figure S1). The presence of water in the cavity is

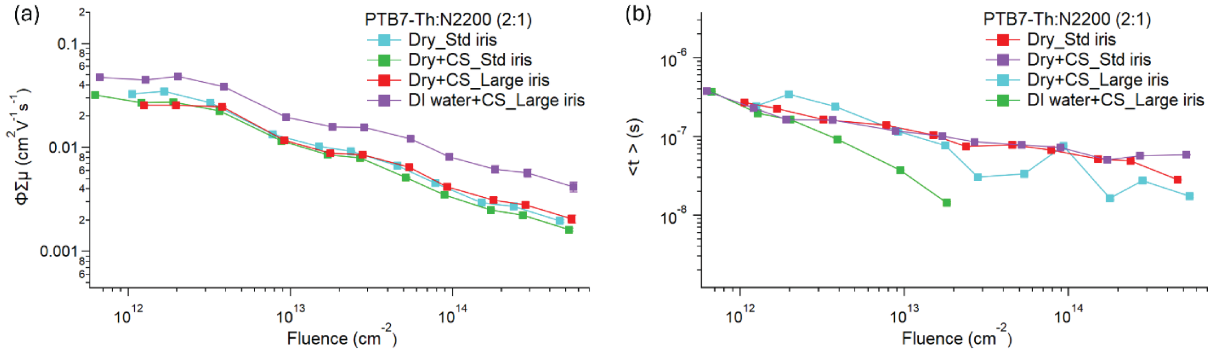


Figure S3: (a) Yield-mobility products across different fluences for PTB7-Th:N2200 (2:1) blend samples in presence and absence of cover slip (CS) and different size iris of the cavity. The cavity was modeled in COMSOL for different iris sizes and inclusion of CS which resulted in agreement of the $\phi\Sigma\mu$ data for the dry sample with or w/o CS and with various iris sizes.

easily detected by the changes it produces in resonance frequency, depth, and width of the microwave cavity. To illustrate this, the impact of water evaporation on the microwave cavity resonance is depicted in Figure S2.

Introduction of the cover slip and water to perform *in-situ* experiments also resulted in a reduction in the quality factor of the microwave cavity. In order to accommodate these changes with optimal measurement sensitivity, the coupling iris that forms one end of the cavity was increased from our usual configuration ($d = 9.8$ mm) to $d = 11.5$ mm. Electromagnetic simulations (COMSOL Multiphysics) were performed to calculate the sensitivity factor (K-factor) of the cavity in this new configuration with wet samples. In the simulations, we represent the whole sample system including polymer film, water, cover slip and grease sealant with a single slab of effective medium with a single conductance (G) and relative dielectric constant (ϵ_r). A lookup table of simulated cavity characteristics was created for a wide range of effective conductance and dielectric constants ($G = 0 - 1e-3$, $\epsilon_r = 3 - 9$) and then fit to the characteristics of a given sample to determine the K-factor, which is given by the partial derivative of power reflectance with respect to conductance at the point in the lookup matrix that best matches the experimentally observed cavity characteristics.^{2,3} This

procedure was necessary for every sample because it was not possible to adequately control the amount of water present such that a single K-factor could be used. In general, the value of K was $\sim 7,000 \Omega$ with a thin-film of water present. To verify the ability of this modeling procedure to account for changes in cavity characteristics, TRMC transients were recorded for a single sample using several measurement configurations: (1) standard iris, (2) standard iris and cover slip, (3) enlarged iris and cover slip, (4) enlarged iris, cover slip, and water. If the simulations are successful in capturing the differences in cavity characteristics all of these changes entail, then all of these measurements except (4) should provide identical results. (4) with water may differ if the water leads to real changes in the photoconductivity of the sample.

Figure S3 shows fitting results to these data giving the yield mobility product ($\phi\Sigma\mu$) and average lifetime for different fluences. The results show that with the CS and large iris, polymer blend results in overlapping $\phi\Sigma\mu$ and average lifetimes for all except the sample with water (Figure S3a,b).

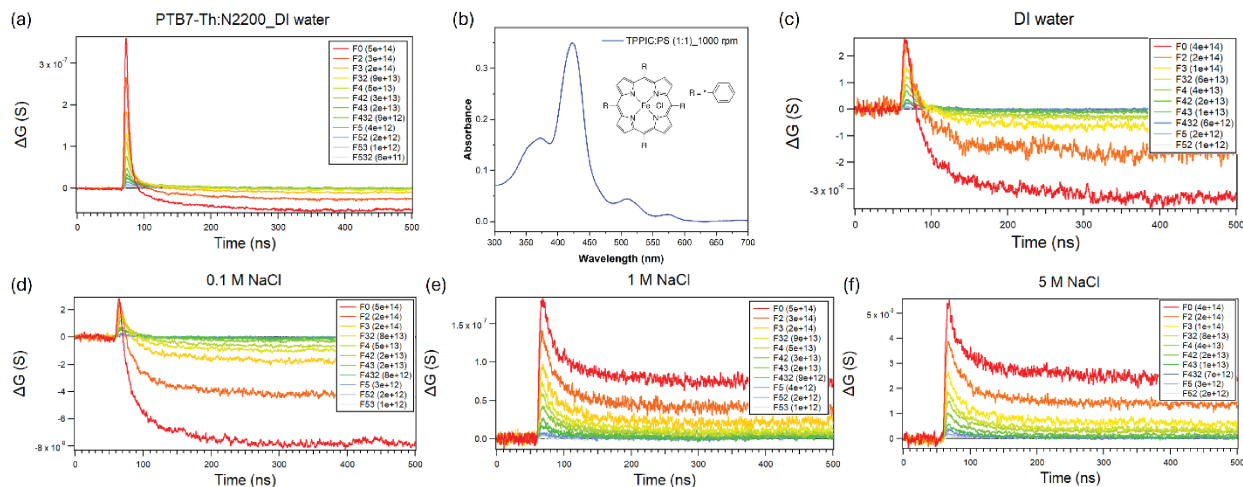


Figure S4: (a) *In-situ* TRMC photoconductance transients of PTB7-Th:N2200 in presence of DI water; (b) thin film UV-visible absorbance spectrum of TPPIC:PS (1:1) spun from toluene (20 mg/mL) solution at 1000 rpm; in situ TRMC photoconductivity decay transients of TPPIC:PS in (c) DI water, (d) 0.1 M NaCl, (e) 1 M NaCl and (f) 5 M NaCl.

The influence of water or electrolyte on TRMC measurements extends beyond special requirements for cavity calibration. It turns out that the heat deposited by the laser pulse also leads to transient changes in the dielectric loss of the high dielectric constant media,² which appears as a spurious contribution to the conductivity of samples measured *in-situ*. We control for the influence of this behavior through different control experiments for TRMC and SSMC experiments. For TRMC experiments we investigated the magnitude of these “thermal artifact” signals using iron tetra-phenyl porphyrin (5,10,15,20-Tetraphenyl-21H,23H-porphine iron(III) chloride, TPPIC) dispersed in polystyrene (1:1 by weight, TPPIC:PS). This molecule converts excited states to heat within 20 ps,⁴ making it ideally suited for investigating transient heating here. Figure S4 shows a comparison between PTB7-Th:N2200 and TPPIC:PS samples in various electrolyte environments, as well as the absorbance spectrum of the TPPIC:PS sample in Figure S4b. The excitation wavelength was 420 nm for these experiments to obtain similar optical densities for the PTB7-Th:N2200 and TPPIC:PS samples. The TRMC ΔG transients of the TPPIC:PS in DI water, 0.1 M, 1 M and 5 M NaCl are exhibited in Figure S4. For comparison, ΔG decay transients of PTB7-Th:N2200 are shown in Figure S4a. For the lowest fluences, e.g. $2\text{E}12\text{ cm}^{-2}$, the ΔG_{max} for PTB7-Th:N2200 is $2\text{E}-8\text{ S}$, which is close to two orders of magnitude higher than the TPPIC:PS sample in DI water (Figure S4c). Interestingly, the shape and intensity of the transient change in dielectric loss varies as a function of electrolyte concentration, but in all cases it declines more rapidly as a function of excitation fluence than does ΔG_{max} for PTB7-Th:N2200. As a result, the low-fluence region of the PTB7-Th:N2200 is virtually free of these artifacts. The resonance curves of the microwave cavity with encapsulated blend samples is shown in Figure S20, this shows the sensitivity of the cavity to the change in sample environment.

The original methodology for conducting TRMC experiments on semiconductors in contact with water was developed in the Ardo lab at UC Irvine, and although the systems investigated there (TiO_2) are distinct from the polymer photocathodes that are the main subject of this paper, they nevertheless provide another useful reference point. Here we

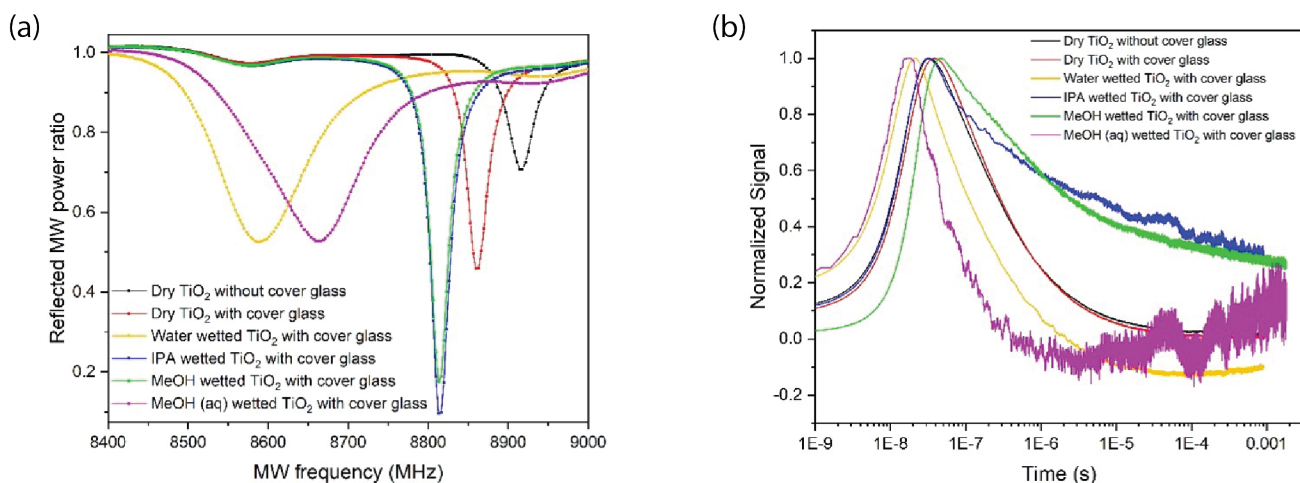


Figure S5: (a) Microwave power reflectance vs. frequency for the dry and wet TiO₂ samples. (b) Normalized TRMC results of dry and wetted anatase TiO₂ samples, each measured at the corresponding resonant frequency.

attempted to probe the photoconductivity of wet TiO₂ samples, which serve as model photoanodes that might be paired with polymer photocathodes in the future.

Commercial anatase TiO₂ (US Research Nanomaterials) was dispersed in isopropyl alcohol, dropcast onto a quartz substrate and dried in air overnight. The substrate was then further annealed to sinter the particles onto the quartz. Anatase samples were wetted by adding a constant volume of solution (DI water, isopropyl alcohol, methanol, or 10 v/v% aqueous methanol solution) to the anatase surface, and using a glass cover slip to encapsulate the sample, as already described above.

The variation in microwave cavity characteristics as first a cover slip, and then high permittivity solvents are added on top of the TiO₂ are shown in Figure S5. By choosing the corresponding resonant frequency in each case, similar signal-to-noise was achieved for each measurement, with the exception of water-based solutions (DI water and aqueous methanol solution). Figure S5 (b) shows the transients obtained with 355 nm excitation of the TiO₂ for each sample condition. The addition of the cover glass (black vs red) does not significantly affect the TRMC transient. Significantly lower signals were observed with water-based wetted

particles, consistent with the reduction in sensitivity factor we have noted in the polymer photocathode work described above. These data were not calibrated using COMSOL as described for the polymer photocathodes, and we thus present normalized results to allow for transient lifetime comparisons.

We observe that when isopropyl alcohol and methanol (blue and green) are used, the transient photoconductivity has a *much* longer lifetime as compared with the dry samples or those in contact with water. This confirms that these signals arise from mobile electrons in the conduction band of the TiO_2 . Isopropyl alcohol and methanol are both common sacrificial hole scavengers used in photocatalysis, and when they are oxidized at this model photoanode it leaves mobile electrons orphaned in the TiO_2 where they are detected via microwave absorption. In contrast, DI water and aqueous methanol (yellow and purple) wetted anatase samples had a shorter lifetime than the dry films, and both transient peaks were shifted to earlier time scales compared to dry particles. Moreover, the transient signals cross through zero and become negative after $\sim 1 \mu\text{s}$. These results are explained by a combination of effects. The presence of water dramatically reduces the quality factor of the microwave cavity, allowing it to respond faster, and accounting for the earlier sharper peak observed for electronic photoconductivity in the TiO_2 . Simultaneously, the thermal artifact observed above for the high-fluence measurements on polymer photocathodes and the TPPIC:PS may explain the very long-lived negative contribution that becomes observable after the photoconductivity of the TiO_2 has decayed.

1.8 Steady State Microwave Conductivity (SSMC)

In-situ steady state microwave conductivity (SSMC) experiments were performed using the experimental setup described previously.⁵ Briefly, the samples were illuminated by a white LED source with a spectral range of 400-800 nm with flux close to $5 \times 10^{16} / \text{cm}^2$. The light was electronically chopped using a transistor wired in the ground path, and a frequency sweep was performed from 1 Hz – 20 kHz to investigate the ms timescale kinetics of the

photoconductivity. A lock-in amplifier (SR830) was used to resolve both the phase and amplitude of the reflected microwave signal w.r.t. an internal reference. A manual shutter was used, and a dark signal was also recorded for each sample with the tuned circuit so that pure electronic interference could be subtracted as described for the steady-state photoinduced absorption measurements below. The samples were prepared using the schematic described in Figure S1 and were placed inside the same microwave cavity used for TRMC experiments. The cavity voltage and open cell voltage were recorded, and the calibrated detector was used to calculate the respective microwave power, the ratio of which is the power reflection coefficient. Assuming similar type of Lorentzian function as obtained for TRMC and with the depth of the function as power reflection coefficient, K-factors were calculated for the samples with water/electrolyte solutions exactly as described for the TRMC experiments, above.

A fast photodiode placed at the sample position collected signal from the pump as a function of frequency. We used this to phase-correct the SSMC signal as described for Steady State Photoinduced Absorption (SSPIA) (see below).

Neat N2200 films were used as control samples to detect changes in apparent photoconductance due to thermal artifacts. N2200 has a similar optical absorbance spectrum to the blend, but does not readily generate charge carriers.^{6,7} Thus, changes in photoconductance with neat N2200 films (shown as empty circles in Figure 2b in the main text) can be attributed to thermal artifacts from the solvent.²

1.9 Transient Absorption

Transient absorption (TA) measurements were conducted using a Ti:Sapphire laser (Coherent Astrella) with a 1 kHz repetition rate and 800 nm fundamental with a pulse width of 100 fs. The beam was split into pump and probe pulses and the pump wavelength was tuned using an optical parametric amplifier (Light Conversion, TOPAS-C). The probe pulse was directed through a multi-pass mechanical delay stage and focused on either of two sapphire

crystals of different thicknesses, depending on whether a visible (440-840 nm) or NIR (850-1500 nm) probe was used, and split into sample and reference beams. The reference beam was directed to a fiber coupled multichannel spectrometer with a CMOS sensor to maximize the signal-to-noise ratio. Meanwhile, the pump and probe beams were spatially overlapped at the sample, after which the probe was directed to another fiber coupled multichannel spectrometer to monitor changes after photoexcitation. Collection software for ultrafast experiments (-2 ps-5 ns) was provided by Ultrafast Systems (Helios). For ns- μ s measurements, an electronically delayed continuum fiber laser (Ultrafast Systems, EOS) was used to generate the probe pulse, while the pump remained the same as the ultrafast experiments. All measurements on films were conducted with a pump pulse energy of 40 nJ. The pump spot size was on the sample kept constant at 330 square microns.

1.10 Sample Prep for TA

Polymer films were spin-coated onto quartz substrates as described previously. The slides were mounted on a two-inch-diameter, 2-mm-thick window using double-sided tape. This window was then inserted into a sample holder consisting of a two-inch beam tube, a Buna-N o-ring coated in vacuum grease, a 1-mm-thick window, and another locking ring. Depending on the required conditions, the sample was either assembled in the glovebox or in air. For experiments involving the films in aqueous media, the films were soaked in distilled water, a mixture of 0.1 M sodium sulfate and 0.1 M sulfuric acid, or 5 M sodium chloride for an hour, followed by mounting on the window in the sample holder, filling the holder with the appropriate solution, and sealing with the second window and locking ring.

1.11 Steady State PhotoInduced Absorption (SSPIA)

A 640 nm diode laser from Toptica was used as the pump and a monochromated xenon lamp was used as the probe (75W, Tuneable Power Arc, BBO/Horiba). A New Focus 2317 NIR

photodiode was used to detect transmitted light. A UHF Zurich lock-in amplifier provided the trigger for modulation of the pump while also detecting ΔT between the on and off conditions and recording total transmitted light, T , *via* voltage from the photodiode. In-house-built software was used to control the experiments and to process the data sets of complex numbers produced by the experiment.

Briefly, a ground-glass disk was inserted *in lieu* of a sample and illuminated at a fixed probe

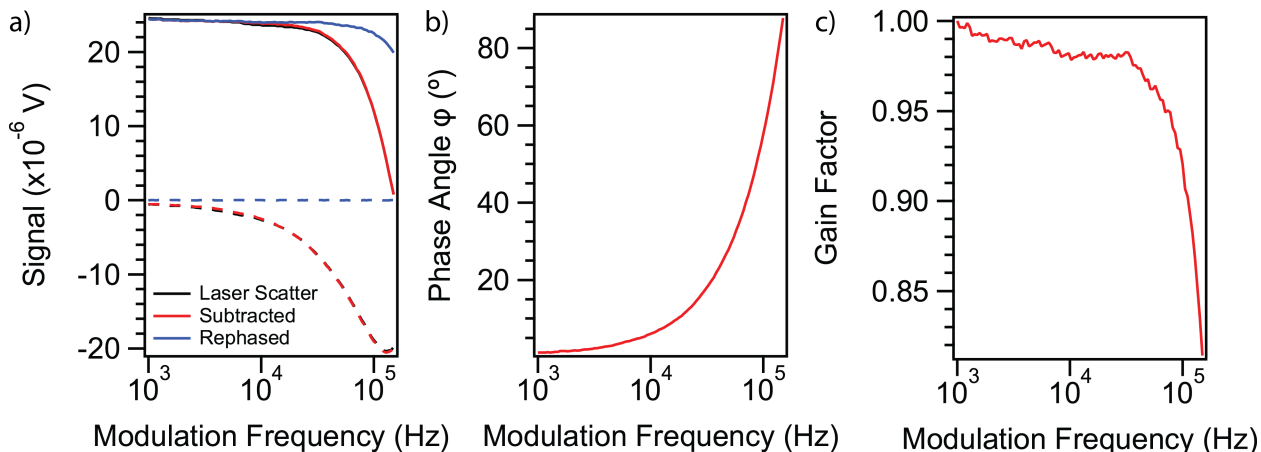


Figure S6: (a) Laser scatter measurements (black) with subtraction of background electronic noise (red), phase-corrected so that the entire signal is in-phase (blue). X-channel (in-phase) signals are shown as solid lines, Y-channel (out-of-phase) as dashed. (b) Optimized phase angles to put the entire signal in-phase as a function of modulation frequency. (c) Frequency-dependent detector gain factor.

wavelength of 1150 nm. A range of pump frequencies from 1 kHz to 150 kHz was scanned on the lowest gain setting both with the pump hitting the probe spot on the ground glass disk and with the pump obscured by a beam-block. The signal with the pump blocked was treated as the electronic noise inherent in the setup and subtracted from the detected pump scatter with the pump beam unblocked. Then, the pump scatter was rephased at each frequency point as in the literature⁸ by iteratively multiplying by $e^{i\varphi}$, where φ is the phase angle from a set between 0° and 180° , and taking the φ giving the greatest amount of signal in the X channel (the real part of the complex signal). Finally, a curve of optimized phase angles vs. frequency was constructed and used to phase-correct constant-frequency wavelength

scans in order to account for any time delay introduced by the electronics. One should note that, in our phase reference data (the laser scatter measurements described previously), the signal magnitude $R = \sqrt{X^2 + Y^2}$ declines with frequency. Thus, for frequency-dependent measurements, we applied an additional correction factor to the data for the frequency-dependent gain, $A(f) = R(f)/R_0$.

Samples were again mounted in the holder used for TA experiments, though the solutions had to be sparged with nitrogen prior to use. Thus, during soaking of the samples, house nitrogen was bubbled through the aqueous medium, again for a period of one hour. The sparged solution was used to fill the sample holder after mounting the sample.

1.12 X-Ray Reflectivity (XRR)

XRR determines the thickness of samples based on interference patterns in reflected X-rays. XRR samples were prepared by spin-coating polymer films onto 10 x 10 mm silicon substrates (University wafers) following the method described above. *In-situ* XRR data was collected using a Rigaku SmartLab instrument with a copper anode source and length limiting apertures of 5 mm horizontal and 0.05 mm vertical. A custom humidity cell (Figure S7a) was constructed based on a previous design was used.⁹ The sample chamber consisted of a polyether ether ketone (PEEK) body with a stainless steel frame that held Kapton windows and a fluorosilicone gasket fastened to the body with screws to hold the sample in a sealed compartment. This allowed for control of relative humidity (RH) in an inert environment. To vary the RH in the sample chamber, a partial pressure delivery system was used based on a previous design.¹⁰ Dry N₂ gas was split to two Alicat MC series mass flow controllers (MFCs) which were used to set a total constant gas flow of 1000 sccm. The first MFC delivered dry N₂ gas directly to the sample chamber to measure sample thickness in 0% RH atmosphere. The second MFC delivered gas through a glass bubbler (Corning™ PYREX™ brand) to carry saturated water vapor to the sample chamber. A Honeywell humidity sensor (model: HHH-4021-004) with an accuracy of ±3.5% RH measured the RH

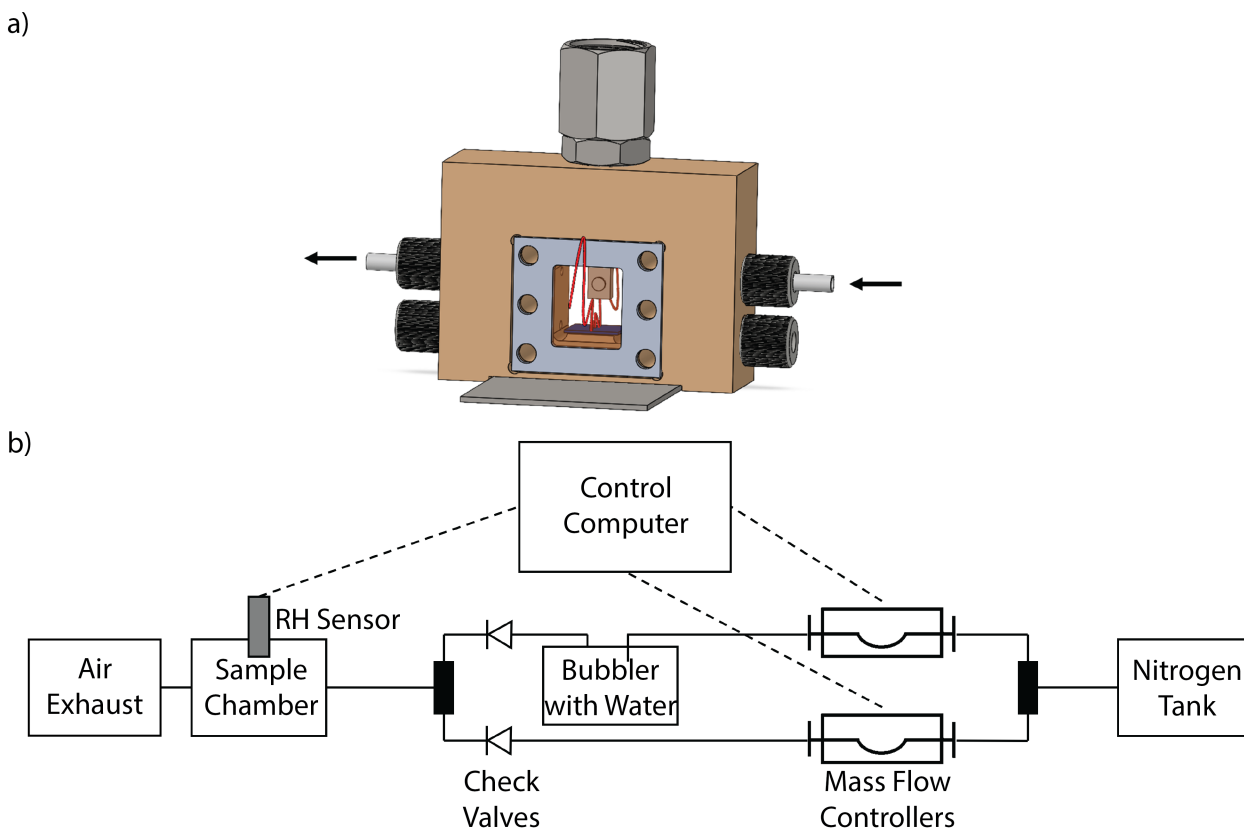


Figure S7: *In-situ* humidity chamber for XRR measurements. (a) Sample chamber schematic showing the direction of gas flow with arrows. (b) Schematic depicting method for controlling RH in the XRR sample chamber by delivering dry N₂ gas or by bubbling N₂ carrier gas through a water reservoir.

in the sample chamber. A schematic of the gas delivery system is shown in Figure S7b. The sample was first measured at ambient conditions (22% RH) outside of the cell (*ex-situ*). The sample was then soaked in water for one hour, briefly dried using compressed air to remove the water droplets, and measured in the *in-situ* sample chamber at 94% RH.

The raw data was normalized, and fits were performed using GenX3.¹¹ A square beam footprint correction was used with a beam size of 0.05 mm and a sample length of 10 mm. The raw data and fits are shown in figure S8 and indicate swelling of 2.3%. The silicon substrate and native silicon oxide layer had electron density values of ca. 2.42 g cm⁻³ and

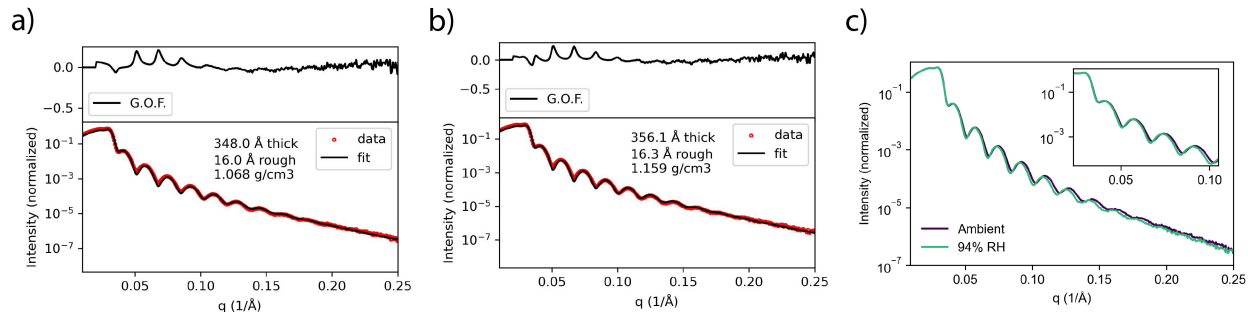


Figure S8: Fit curves derived using GenX3 used to extract volumetric data for the swelling of the PTB7-Th:N2200 blend. (a) Data, best-fit-line, and residuals for the film in ambient conditions. (b) Data, best-fit-line, and residuals (G.O.F.) for the film in 94% relative humidity after an hour of soaking in water. (c) A comparison of the data for the film measured in ambient conditions and the soaked film in 94% RH.

2.70 g cm⁻³, respectively.

1.13 Grazing-Incidence Wide-Angle X-ray Scattering (GIWAXS)

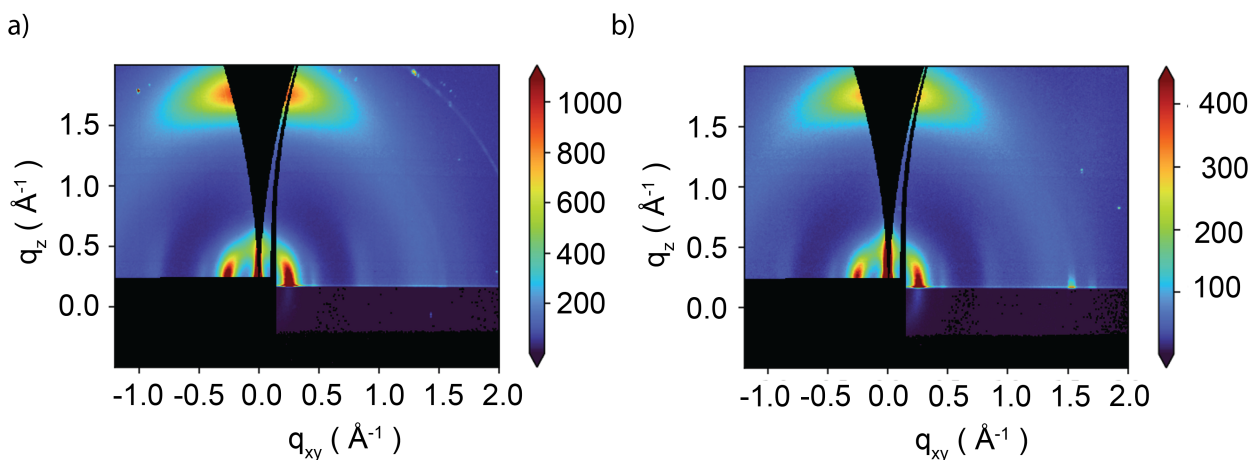


Figure S9: Raw data from the GIWAXS experiments conducted on PTB7-Th:N2200 blend films (a) after soaking with water and without soaking with water. (b) NaCl electrolyte of varying concentrations was used as well, but did not show a clear concentration trend.

Films for X-Ray diffraction were prepared identically to those described in the sample

preparation section. GIWAXS measurements were conducted at 11-BM, Complex Materials Scattering (CMS) at National Synchrotron Light Source II (NSLS-II) at Brookhaven National Lab (BNL). Data were acquired at an incident angle of 0.08° with an exposure time of 1 second. Samples were measured under vacuum. The data shown in Figure S9 were used to produce the 1D integrated linecuts shown in Figure S10.

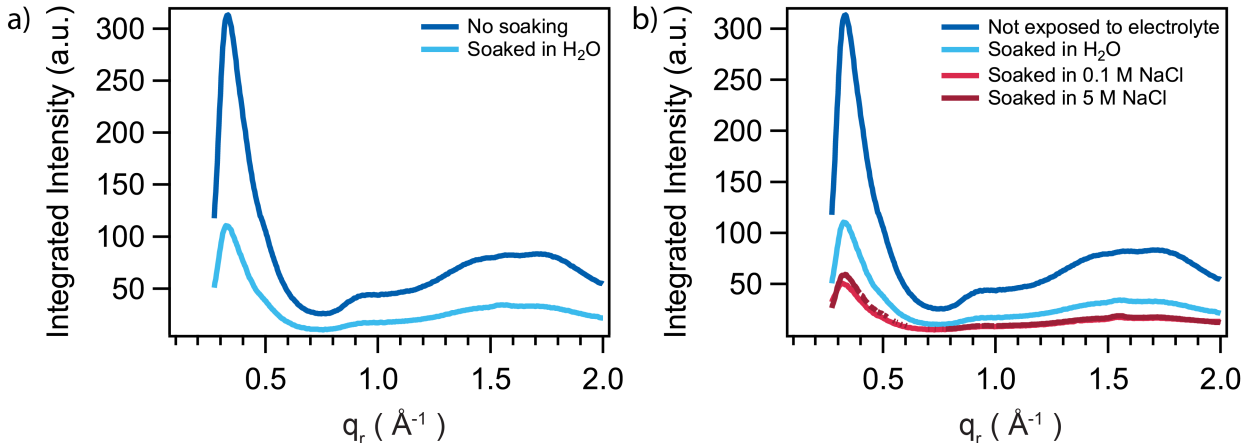


Figure S10: Radially-integrated linecuts of the dry blend film and a blend film soaked in water for an hour prior to measurement in a high-vacuum chamber. Note the drastic change in peak height for films that are of similar thickness (within 10%), indicating a large reduction in ordered regions capable of scattering x-rays.

1.14 Computational Methods

DFT and TDDFT calculations were performed with a long-range corrected hybrid functional LC- ω HPBE, optimally tuned (gap tuned) with respect to both the HOMO and LUMO, and the 6-31G(d) basis set using the Gaussian 16 Rev. A.03 software suite. Geometry optimizations for neutral and charged polymers with side chains truncated to methyl groups were carried out. The polarizable continuum model (PCM) was used represent dielectric effects on the chain in the polymer bulk [$\epsilon=2.7$] and in water [$\epsilon=78.4$]. The optimized geometries were subsequently employed as the input for TDDFT calculations. Excitation energies and oscillator strengths were obtained, and an artificial broadening of $\sigma = 0.3$ was applied to each peak to simulate the optical absorption spectra.

Comparison between the experimental and theoretical spectra of the neutral polymer was used to identify key peaks and shows that results from the DFT calculations appear blue shifted in comparison. To replicate the TAS results for the N2200:PTB7-Th film exposed to N₂, an implicit solvation model is used to create an environment representative of a polymer film, while for the film exposed to water we use water as our implicit solvent. By comparing the calculated absorbance spectra of the two we see that most peaks that appear in the region of interest change minimally. However, the N2200 P1 peak does blue shift going from 1.2 to 1.7 eV in the bulk and water respectively (Figure S34). Together this suggests that the appearance of the low energy peak seen in the dry film and its subsequent disappearance once solvent has been introduced is a result of a shift in the polaron absorbance features for N2200. See Section 3.11 for further discussion.

2 Addressing Potential Confounding Variables

2.1 Pd Removal Procedure

Table S1: Pd content analysis in polymers from ICP-MS.

Polymer Samples	Pd:polymer (ng/mg, ppm)
N2200 before cleaning	1381
N2200 after cleaning	23
PTB7-Th before cleaning	1141
PTB7-Th after cleaning	101

The as-received polymers were found to have parts-per-thousand levels of residual palladium (Table S1). Following a literature procedure,¹ we dissolved the polymers (50 mg) to be purified in 15 mL chloroform and added to an aqueous solution of sodium diethyldithiocarbamate trihydrate (0.205 g, 0.78 mmol) in water (20 mL). The biphasic mixture was vigorously stirred at reflux for 16 h followed by separating the organic layer and concentrating to get the polymer. Finally, the polymer was redissolved in minimum amount of chloroform and reprecipitated from methanol and dried in high vacuum overnight. Elemental analysis from

inductively coupled plasma-mass spectroscopy (ICP-MS) of the treated samples showed a reduction in palladium content to 101 and 23 ppm for PTB7-Th and N2200, respectively (Table S1).

2.2 Photophysical Properties of Treated vs. Untreated Films

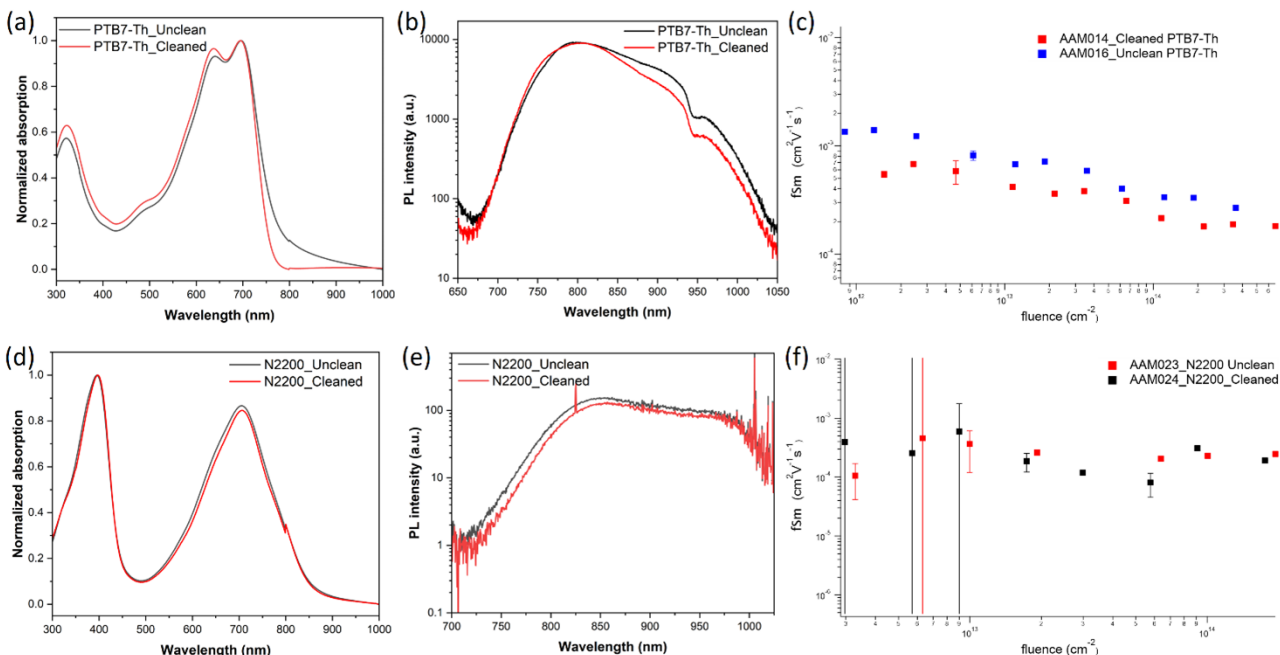


Figure S11: (Top) A comparison of the UV-Vis absorption spectra (a), photoluminescence spectra (b), and TRMC $\varphi\Sigma\mu$ (c) of PTB7-Th having undergone the cleaning procedure (black) and not having undergone the cleaning procedure (red). (Bottom) A comparison of the UV-Vis absorption spectra (d), photoluminescence spectra (e), and TRMC $\varphi\Sigma\mu$ (f) of N2200 having undergone the cleaning procedure (black) and not having undergone the cleaning procedure (red).

Thin films of PTB7-Th and N2200 purified by this procedure were spun-cast from solutions in ortho-dichlorobenzene (16 mg/mL) and compared to thin films of polymer that had not undergone this treatment process. The treated and untreated samples showed identical decay kinetics from time-resolved microwave conductivity (TRMC) experiments. Additionally, the quantum yield of fluorescence for the treated and untreated samples was determined and found to be similar regardless of treatment (1.1% for untreated vs. 1.6% for

treated PTB7-Th). UV-visible absorption spectra and PL emission spectra showed negligible changes as shown in Figure S11a, S11b, S11d and S11e. The fluence dependent yield-mobility products extracted from TRMC experiment also resulted in very similar values for cleaned and unclean versions of either of the polymers under investigation (Figure S11c, S11f). In total it appears that the cleaning procedure led to a modest reduction in static quenching of primary excitons in PTB7-Th, and that these quenching events constitute an adventitious route to charge generation: the decrease in yield-mobility product measured via TRMC is commensurate with the increase in photoluminescence quantum yield. However, as the yield-mobility product remains at least an order of magnitude lower than that observed for the PTB7-Th:N2200 blend, we concluded that these effects were of negligible importance to the photophysics of the blend.

2.3 The Impact of Dissolved Oxygen

The dynamics of a blend film in N₂-sparged and unsparged water were measured using ns- μ s EOS-TA. These conditions were chosen as the two extremes in terms of oxygen content, as any added salt should decrease the solubility of molecular oxygen *via* the salting-out effect; thus, the highest O₂ concentration of any of the aqueous media should be found in dI water. Figure S12 shows that nitrogen sparging (removal of dissolved oxygen) leads to a *faster* excited-state decay. In contrast the fs-ps Helios TA results indicated that the most concentrated electrolyte, which should also contain the least amount of oxygen, experienced the least decay on the 5 ns experimental observation window, which is the opposite of the trend one would expect from the present experiment if O₂ were having a substantial impact on the experimental results. Thus, the trends we observe in the TA experiments as a function of electrolyte concentration cannot be explained by any influence electrolyte content may have on dissolved O₂ concentration.

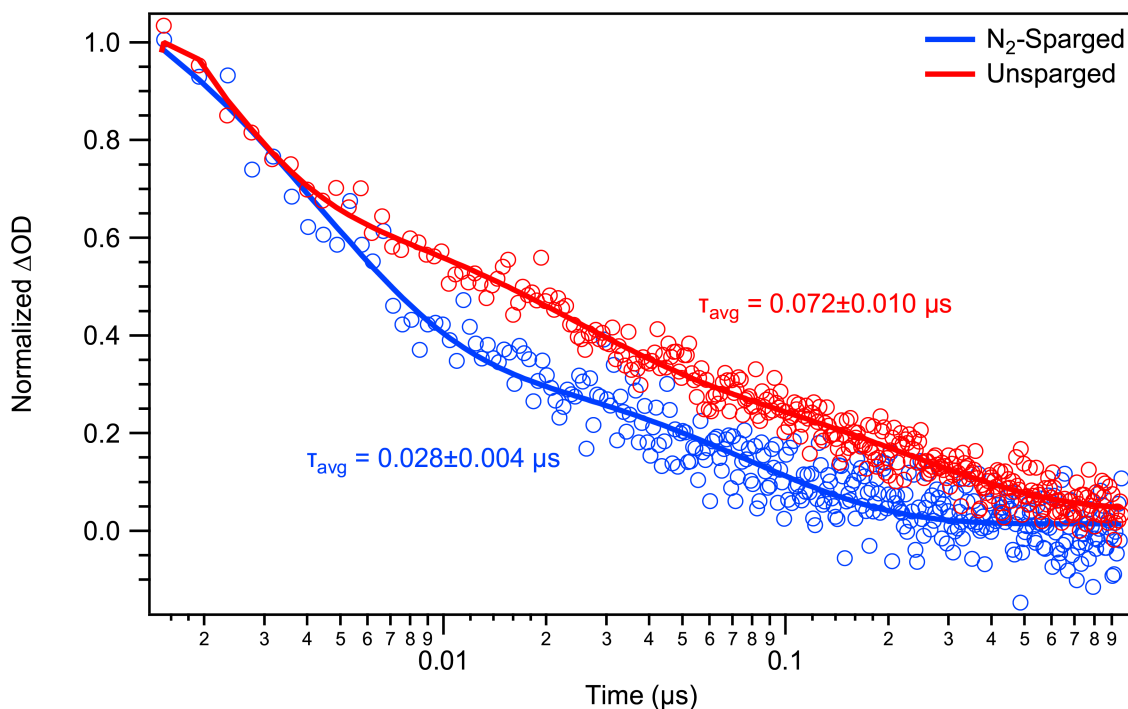


Figure S12: A comparison of the polaron decay dynamics as measured by ns- μ s transient absorption spectroscopy in a blend film in N_2 -sparged (blue) vs. unsparged (red) dI water.

3 Supplementary Data for Main Text

3.1 Profilometry

Table S2 shows the film thicknesses of PTB7-Th:N2200 blend films spin-cast on quartz as measured on a DekTak profilometer.

3.2 Absorbance

Spectra of the individual polymers, as well as the blend, were normalized to the peak near 700 nm. The two individual polymers were scaled, summed, and compared to the blend in

Table S2: Thicknesses (nm) of PTB7-Th:N2200 blend films spin-cast on quartz measured by profilometry.

Spot Number	Film 1	Film 2	Film 3	Film 4
Spot 1	150	130	140	160
Spot 2	150	130	140	160
Spot 3	140	130	140	170
Spot 4	140	130	140	170
Spot 5	150	140	130	140
Spot 6	150	140	130	140
Mean	147	133	137	157
Standard Deviation	5	5	5	14

Igor using least-squares fitting. A linear combination of the N2200 and PTB7-Th films with coefficients of 0.22 and 0.78 matched quite well with the normalized blend spectrum.

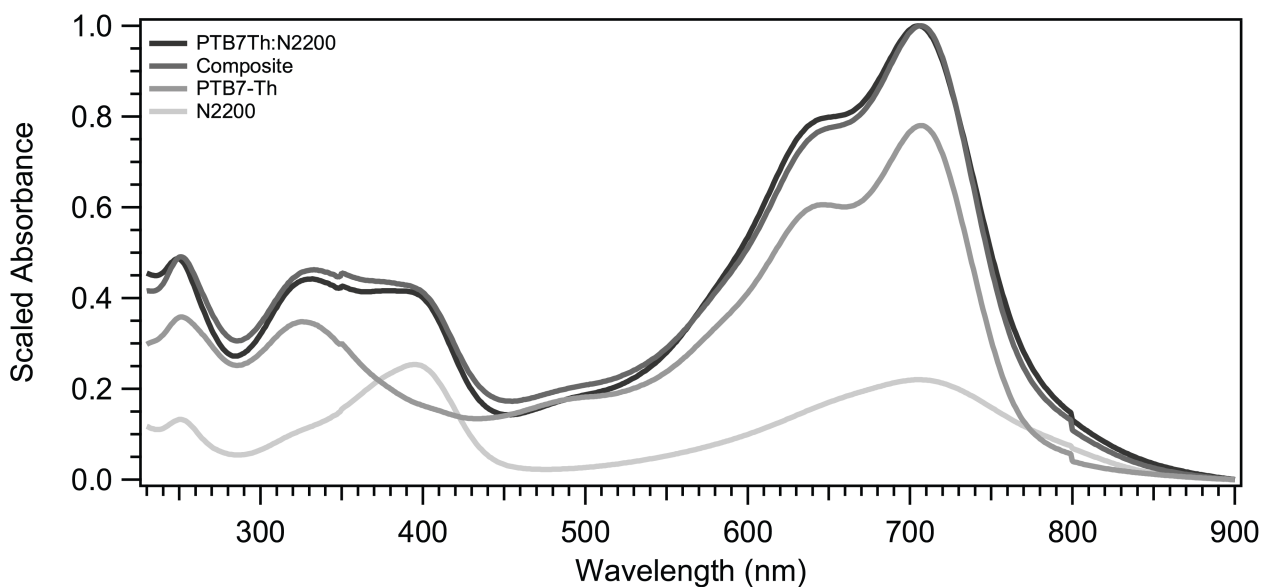


Figure S13: A comparison of the reconstruction of the blend film steady-state absorbance spectrum from its constituent parts, normalized and scaled using least-squares fitting to match the blend film spectrum.

The blend ratio is 2:1::PTB7-Th:N2200 w/w; given this and the molecular weights of the polymer repeat units (989.52 g/mol for N2200, 889.35 g/mol for PTB7-Th) the mole ratio for the repeat units should be 1.8:1. Though this is not the point of this project, it might be handy to note that from this, one can estimate molar extinction coefficient for PTB7-Th

as being roughly double that of N2200 for the lowest-energy absorption band of each.

We performed UV-vis and PL spectroscopy on the PTB7-Th:N2200 samples using the same

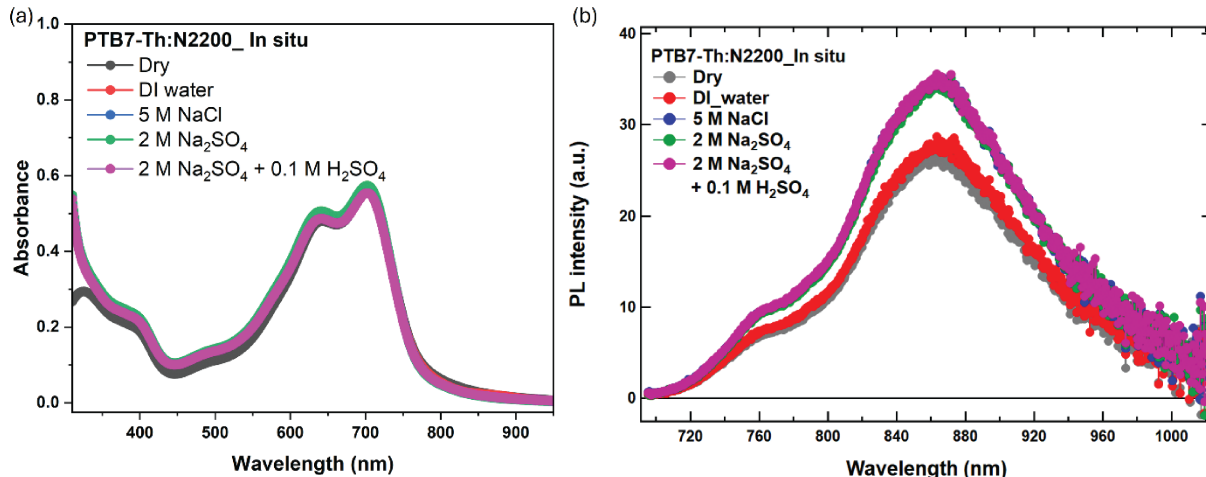


Figure S14: (a) In situ UV-visible absorption spectra of PTB7-Th:N2200 collected in transmission mode; (b) in situ PL emission spectra of the same showing minor change in the intensity of the PL with introduction of water/electrolytes.

conditions as used for microwave conductivity experiments to verify if the effect of change in microstructure detected by GIWAXS is manifested optically. Figure S14 shows the UV-vis spectra of the blend in different aqueous environments which changes negligibly except some broadening which could be due to interference effects because of presence of a thin cover slip very close to the quartz substrate.

3.3 Detection of Absorbed Water by FTIR

The CaF₂ substrate was placed in the sample chamber and the atmosphere purged for 15 minutes before taking a scan. Another was taken after spin-coating with polymer, again waiting for 15 minutes for the atmosphere to purge. 200 μ L of water was then placed on the surface of the polymer which was left for an hour underneath an upside-down beaker in the fume hood. The water was then blown off with a stream of compressed N₂ for \sim 5 seconds, the sample put back in the sample chamber of the instrument, and a scan was taken

immediately. Another scan was taken after 15 minutes of the sample sitting in the chamber with continual purging with N_2 .

The CaF_2 baseline was subtracted from all of the measurements of polymer samples. Figure

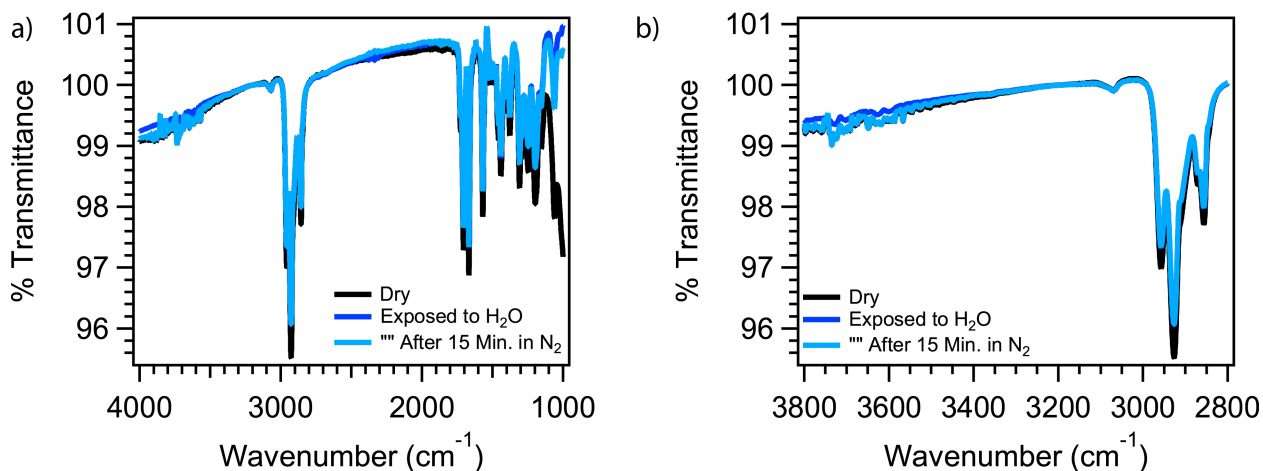


Figure S15: FTIR spectra of the dry polymer blend film on CaF_2 , immediately after soaking with water for an hour, and after purging the sample chamber with N_2 for 15 minutes post-soaking. The full spectrum (a) and spectral region where water would be expected to appear (b, $3200\text{-}3700\text{ cm}^{-1}$) are shown.

S15 shows that there is no detectable difference in the region between 3200 cm^{-1} and 3700 cm^{-1} , where the OH stretches of water would appear.¹² Thus, we conclude that there is no detectable water uptake into the film from soaking using this method.

3.4 Hydrogen Evolution Experiments

HER performances were measured in a three-electrode system. ITO/Me-2PACz/BHJ/Pt, Ag/AgCl/sat. KCl/0.1 M H_2SO_4 (double junction), and $IrO_x\text{-}Ta_2O_x$ -coated Ti plate were used as a working, reference, and counter electrodes, respectively. 0.1 M H_2SO_4 , 0.1 M $H_2SO_4 + 0.1\text{ M Na}_2SO_4$, 0.1 M $H_2SO_4 + 2.0\text{ M Na}_2SO_4$, 0.1 M NaCl, 1.0 M NaCl, and 5.0 M NaCl solutions in DI water were used as electrolytes, respectively. The electrolytes were Ar-sparged for at least 30 min before use. A solar simulator with AM1.5G-filtered Xe lamp (HAL-320, Asahi spectra) and a light chopper was used as the light source. Linear scan

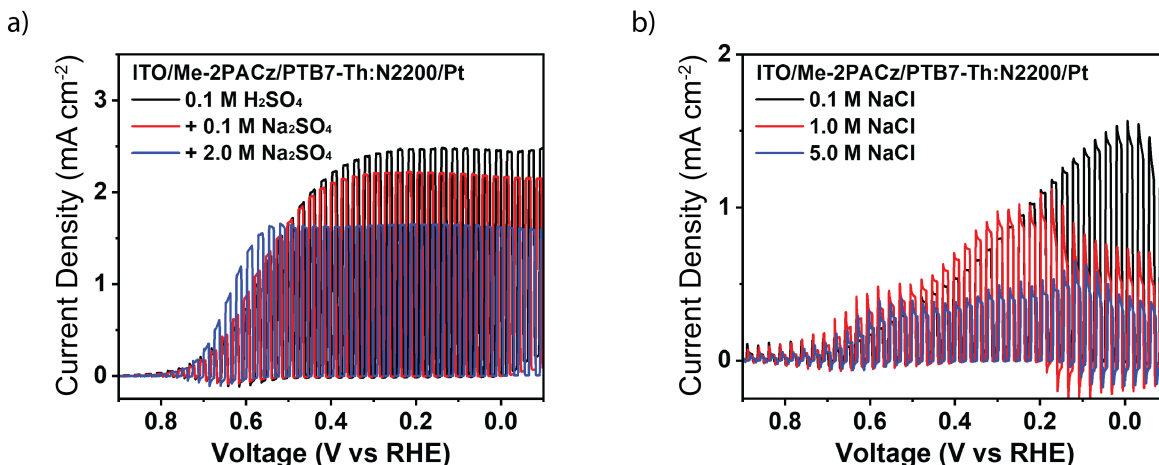


Figure S16: LSV scans of ITO/Me-2PACz/PTB7-Th:N2200/Pt photocathodes in (a) acidic and (b) neutral electrolytes under chopped 1 sun illumination. Data are plotted in the polarographic convention

voltammetry (LSV) scan was performed at a scan rate of 20 mV s^{-1} with an active area of 0.672 cm^2 using a CH instruments 920D bipotentiostat.

3.5 Stability Testing

We performed SSMC and SSPIA measurements on the blend films under continuous irradiation for an hour in order to compare their stability to the stability of the whole photocathode during a chronoamperometry (CA) experiment under illumination. Figure S17b and c show that for the dry films in a nitrogen atmosphere, no degradation occurs. For the films in a $0.1 \text{ M Na}_2\text{SO}_4$ and $0.1 \text{ M H}_2\text{SO}_4$ environment, deemed the most likely to cause degradation due to its acidity, a small amount of degradation on the order of 10-20% occurs over the course of an hour in N_2 -sparged solutions. When oxygen is introduced either by exposing the film to air or not sparging the electrolyte solution, the film degrades to a greater extent. This process occurs continually over the timespan of 20-60 minutes. Figure S17a gives CA data for the whole photocathode under conditions used for HER in electrolyte sparged with Ar. The first 400 seconds of the experiment show a sharp drop in current. Hydrogen bubble formation on the surface of the electrode, blocking portions of the surface from

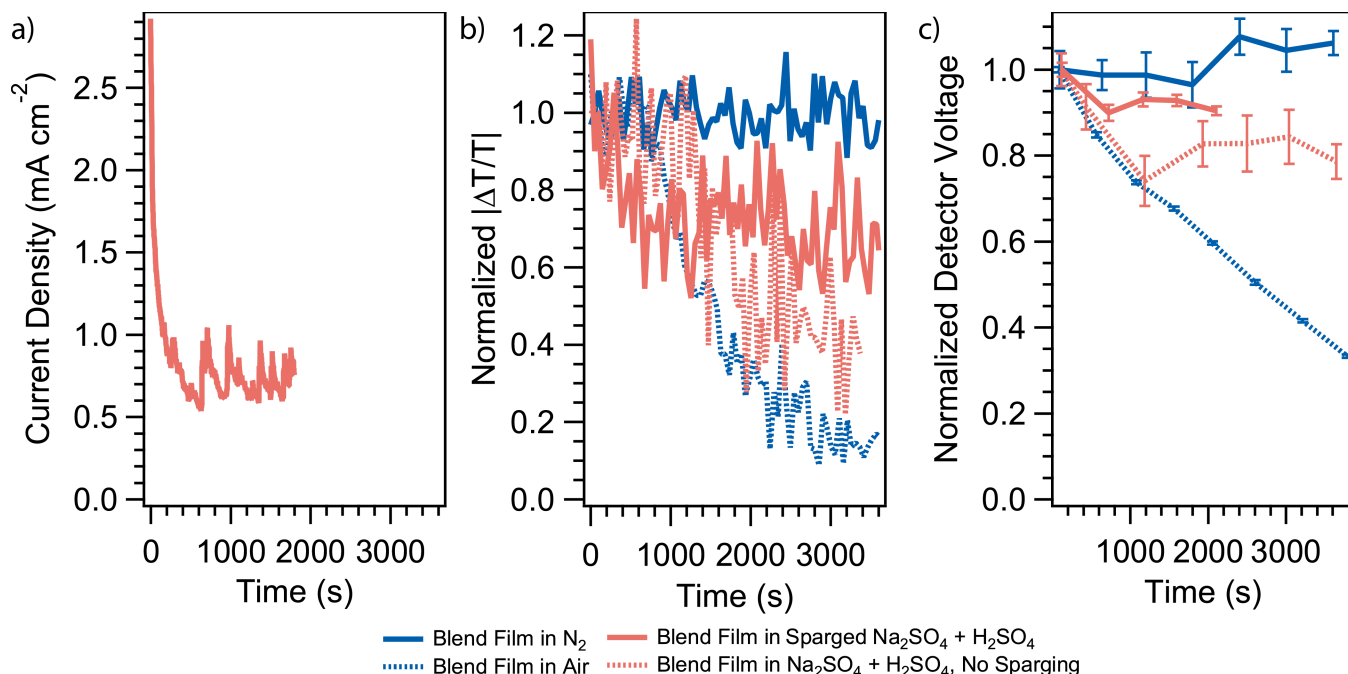


Figure S17: (a) Chronoamperometry data from the photocathode under 1-sun illumination at an applied bias of 0.0 V vs. RHE. The solution was sparged with Ar prior to measurement and the data are plotted in the polarographic convention. (b) SSPIA data showing the normalized magnitude (R) of $\Delta T/T$ at the PTB7-Th radical cation peak over time. N₂ was used for sparging. (c) SSMC data showing the normalized change in the voltage of the microwave detector over time. N₂ was used for sparging.

making contact with the electrolyte and performing HER, is the most likely culprit. The photograph of the photocathode in S18a clearly shows hydrogen bubbles adhering to the polymer and blocking contact with the electrolyte. There may also be contributions from other processes. For instance, surface trap states on the ITO may sap current. Additionally, a current spike at the beginning of the measurement may result from the turning on of the light source, which in turn would change the open-circuit potential, leading to a capacitive current. However, this typically only lasts for a few seconds^{13,14} and not the roughly 400 s seen in these measurements. Depletion of H⁺, limiting the possible photocurrent, may also contribute. We estimate that this is a relatively small contribution based on the magnitudes of the photocurrent and H⁺ concentration. Future work is planned to quantitatively verify this. The current drop is not due to degradation. The absorbance spectra in Figure S18b before and after the linear sweep voltammetry (LSV) experiments depicted in Figure S16

show no differences. Moreover, the fact that the SSPIA and SSMC data show little evidence of degradation under identical conditions with the exception of a small applied bias make it unlikely that additional degradation would occur during the actual HER experiment.

The small jumps in the photocurrent (from 0.5 to 1.0 mA cm⁻²) in Figure S17a are from incomplete detachment of some of the hydrogen bubbles on the surface of the electrode and the subsequent decay of the photocurrent is due to reattachment of hydrogen bubbles to reduce the effective electrode surface area.

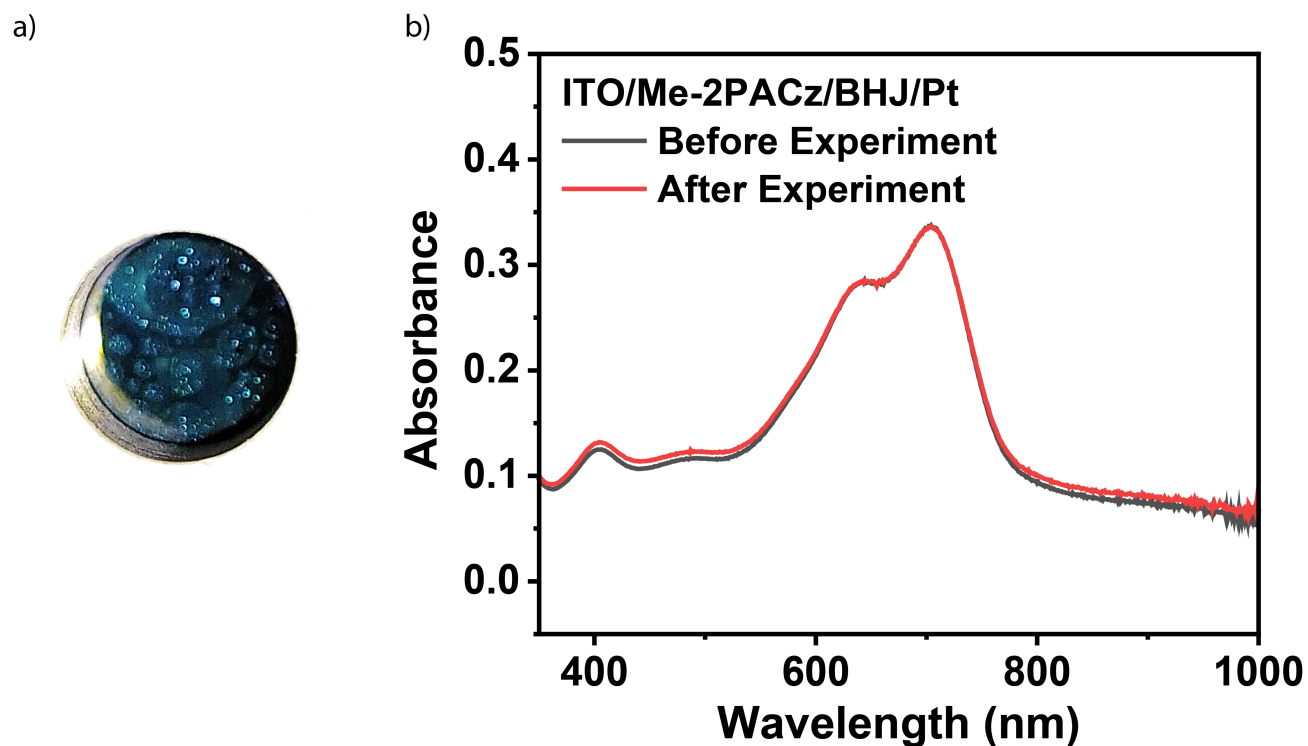


Figure S18: Absorbance spectra of the photocathode used in the stability measurement before and after applying HER conditions for 30 minutes.

3.6 SSMC Frequency Scans

The change in photoconductance (ΔG) for the polymer blend in different conditions in the frequency range of 1 - 20 kHz is shown in Figure S19.

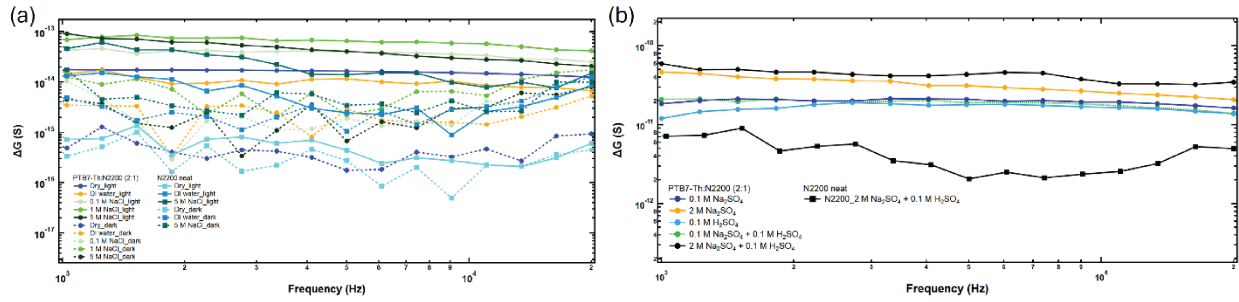


Figure S19: The SSMC photoconductance of PTB7-Th:N2200 in (a) different concentrations of NaCl, the same for neat N2200 as a control is also shown for comparison; (b) different concentrations of Na_2SO_4 with and without acid.

3.7 TRMC Transients

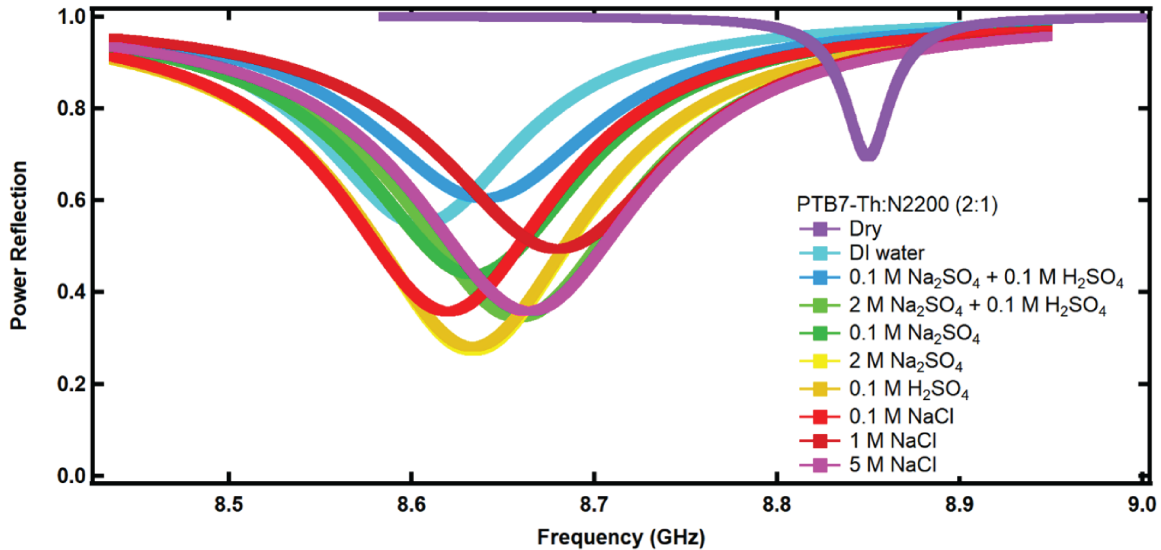


Figure S20: Resonance curves of the microwave cavity with PTB7-Th:N2200 sample in dry and various electrolyte conditions.

The *in-situ* TRMC transients of the PTB7-Th:N2200 in various conditions are shown below. The data are fit using a sum of two-three exponential components numerically convolved with the exponentially-modified gaussian instrument response function, as described elsewhere.¹⁵ In every case the minimum number of exponential components required to adequately fit the data was used. Figure S21 shows the $\phi\Sigma\mu$ transients for the PTB7-Th:N2200 blend in dry, DI water and various concentrations of NaCl. Figure S21 shows the same for

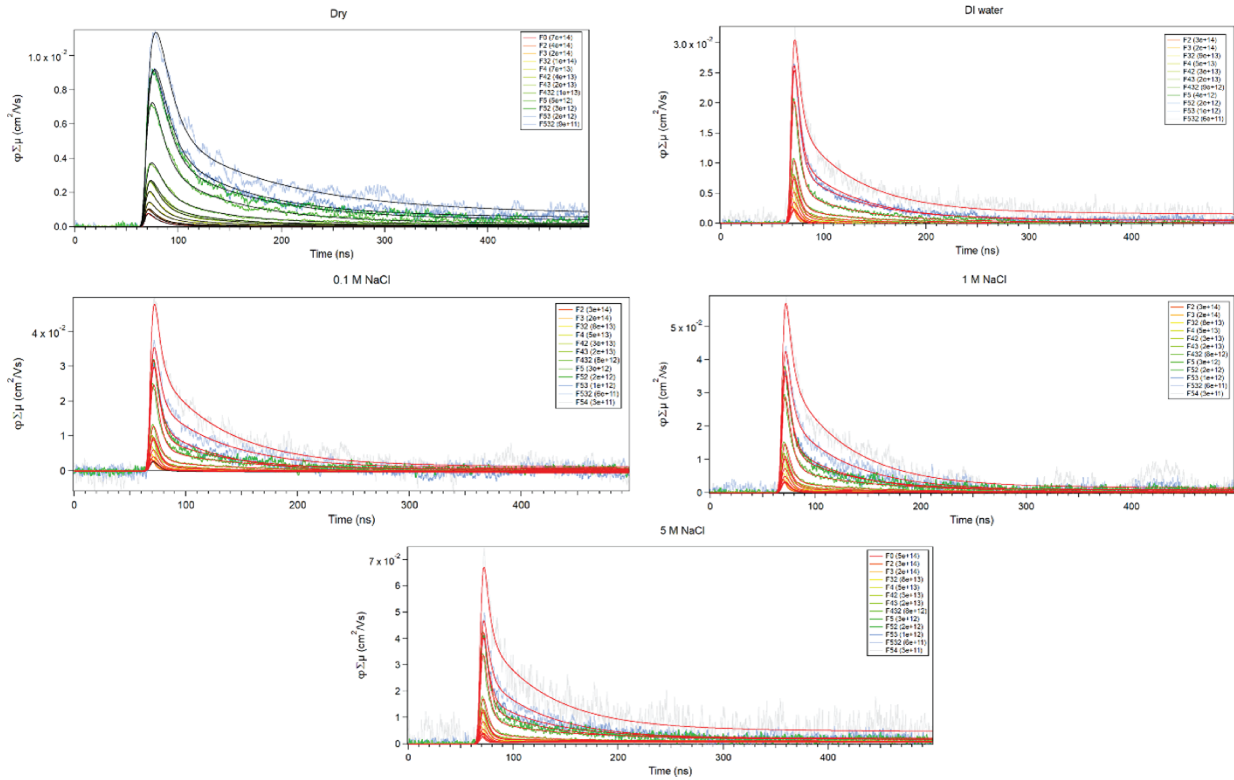


Figure S21: $\phi \Sigma \mu$ transients for the PTB7-Th:N2200 blend in dry, DI water and various concentrations of NaCl. The dark lines overlaid on the original transients are the global fits.

various concentrations of Na_2SO_4 . Ex situ TRMC was performed on the blend samples by treating them with lowest and highest concentrations of electrolytes (NaCl and Na_2SO_4) as well as DI water for 30 mins followed by blow drying using an air gun. The effect of water and electrolyte in enhancing yield-mobility products as well increasing lifetimes was subtle but visible at lowest fluences (Figure S22).

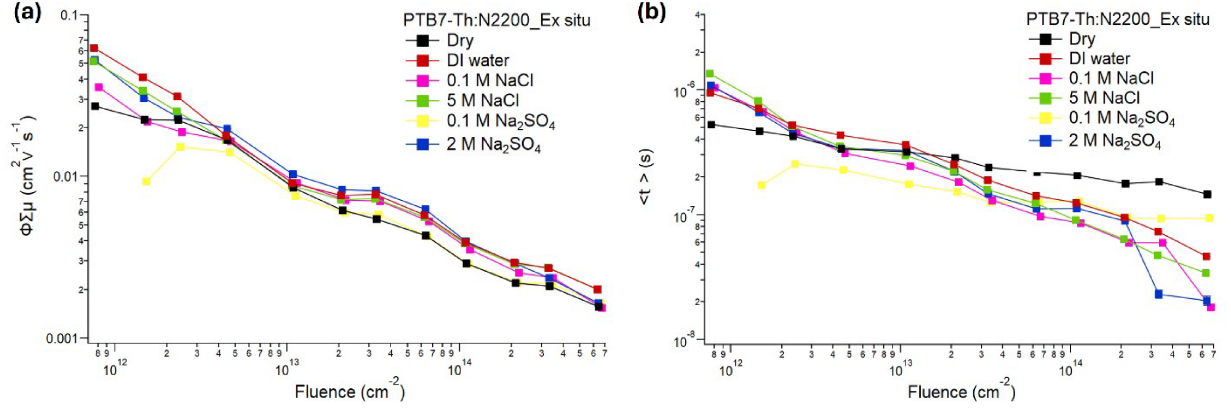


Figure S22: (a) *Ex situ* TRMC yield-mobility product of PTB7-Th:N2200 at various electrolyte concentrations compared with the untreated one, there is a slight enhancement observed for the electrolyte treated sample in lowest fluence. (b) TRMC average lifetime plotted vs. various fluences for the same conditions, the average lifetimes exhibited slight increase in lowest fluences vs the untreated dry sample.

3.8 Additional Discussion of the Dielectric Impact of Water

One can estimate the impact of the change in dielectric environment that would be induced by the small amount of water in the polymer using Marcus kinetics. Many assumptions must be made and the charge recombination process will be more accurately described than the charge separation process due to the distribution of rate constants arising from the large number of available acceptor sites. Analysis will be limited to close ion pairs, as separated charge carrier recombination will likely be governed by polaron diffusion. This analysis nevertheless provides an important point of comparison for understanding how the degree of water swelling we detect in these films *might* impact their photophysical behavior.

The classical correction for driving force (ΔG) in media of different ϵ_r is as follows:

$$\Delta G_{solv} = \frac{e^2}{4\pi\epsilon_0\epsilon_s} \frac{1}{R_{DA}} + \frac{e^2}{4\pi\epsilon_0} \left[\left(\frac{1}{2r_{D^+}} + \frac{1}{2r_{A^-}} \right) \left(\frac{1}{\epsilon_{ref}} - \frac{1}{\epsilon_s} \right) \right] \quad (1)$$

$$\Delta G_{CT} = [e(E_{D/D^+}^{ox} - E_{A/A^-}^{red}) - E_{S1}] - \Delta G_{solv} \quad (2)$$

$$\Delta G_{CR} = [e(E_{D/D^+}^{ox} - E_{A/A^-}^{red})] - \Delta G_{solv} \quad (3)$$

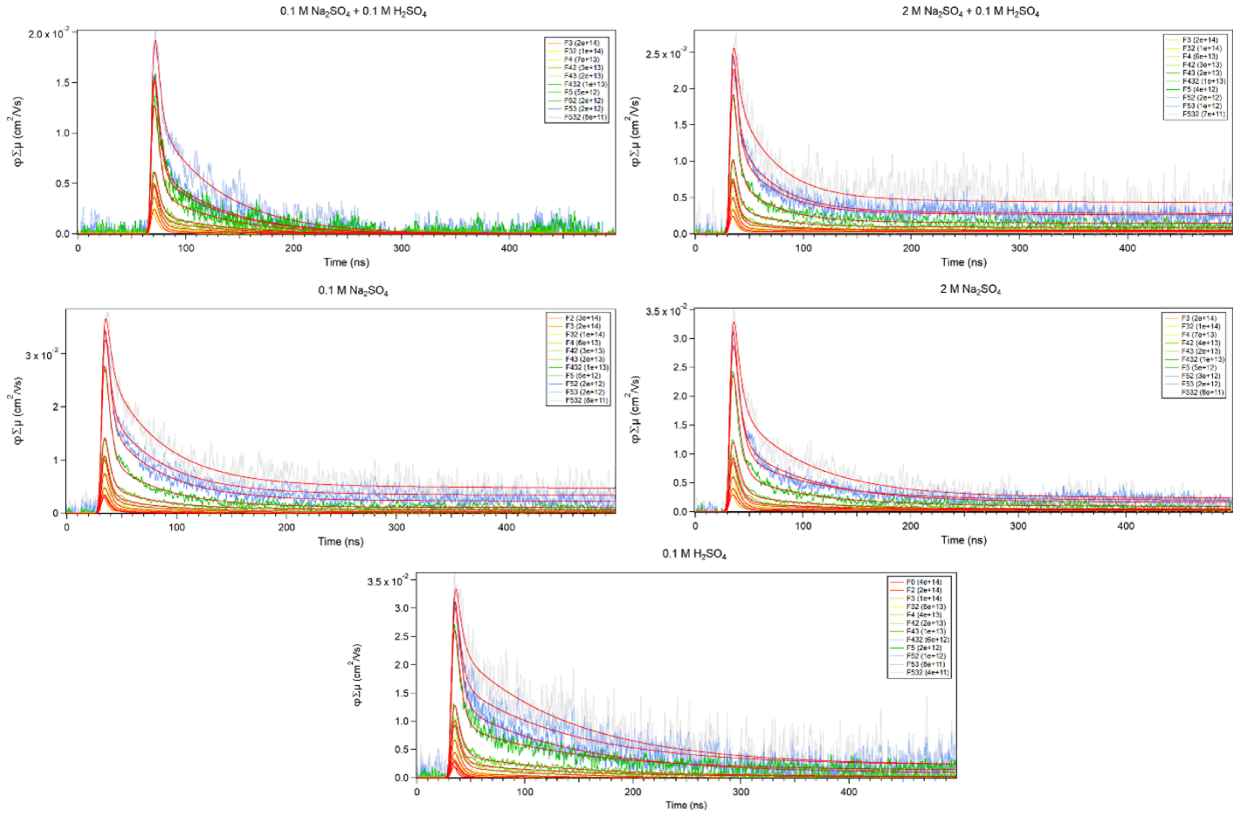


Figure S23: $\phi\Sigma\mu$ transients for the PTB7-Th:N2200 blend in different concentrations of Na_2SO_4 with and without acid. The dark lines overlaid on the original transients are the global fits.

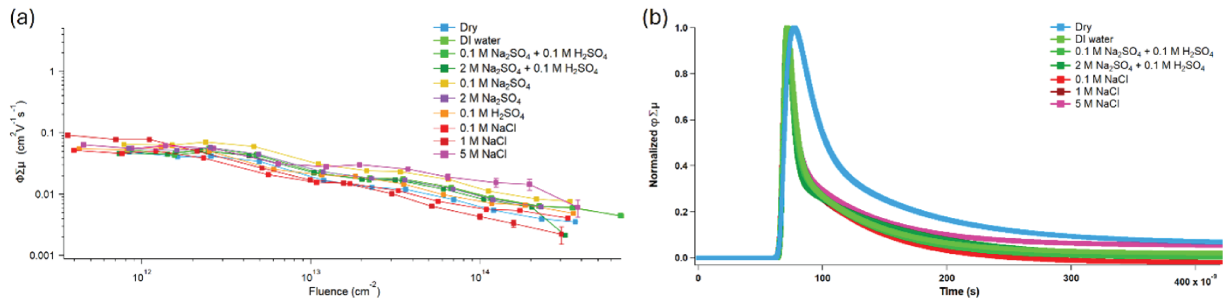


Figure S24: (a) comparison of $\phi\Sigma\mu$ vs. fluence for PTB7-Th:N2200 blend in different conditions, (b) normalized $\phi\Sigma\mu$ decay transients of the PTB7-Th:N2200 blend in different electrolyte conditions. Note that the markedly different appearance of the transient for the dry films is caused by the longer instrument response time connected with the much higher quality factor of the cavity in this case. Fitting the data with the proper instrument response function for each sample shows that the decay dynamics do not vary as a function of water or electrolyte exposure.

Here, e^2 is the elementary charge, ϵ_0 the vacuum permittivity, ϵ_s the relative dielectric constant of the medium, R_{DA} the distance between donor and acceptor, r_{D^+} the radius of the oxidized donor, r_{A^-} the radius of the reduced acceptor, and ϵ_{ref} the solvent in which the redox potentials were measured in by cyclic voltammetry. E_{D/D^+}^{ox} is the oxidation potential of the donor, E_{A/A^-}^{red} is the reduction potential of the acceptor, and E_{S_1} is the energy of the state from which electron transfer is to take place. The Marcus equation to estimate rates is as follows:

$$k_{ET} = \frac{2\pi}{\hbar} |H_{AB}|^2 \frac{1}{\sqrt{4\pi\lambda k_B T}} \exp\left(-\frac{(\lambda + \Delta G)^2}{4\lambda k_B T}\right) \quad (4)$$

Here, \hbar is the reduced Planck constant, H_{AB} the off-diagonal matrix element coupling the two states, k_B is Boltzmann's constant, and λ is the total reorganization energy of electron transfer.

The static dielectric constant of water at room temperature is 78.4.¹⁶ This quantity scales volumetrically.² Thus, if we assume the polymer has a static dielectric constant of ~ 4 , the 2.3% water should contribute 1.80 and the 97.7% contribution from the polymer should contribute 3.91 to the dielectric constant for an effective new dielectric constant of the medium of ~ 5.7 . The following values were used to evaluate equations 1, 2, and 3:

Table S3: Values used to estimate ΔG .

Parameter	Value	Reference
E_{D/D^+}^{ox} (V)	+0.4	17
E_{A/A^-}^{red} (V)	-1.0	18
ϵ_{ref}	7.58	18
E_{S_1} (eV)	1.6	6
r_{D^+} (Å)	5	19
r_{A^-} (Å)	5	19
R_{DA} (Å)	10	N/A

Calculations were also performed for recombination to the triplet state, which is estimated to have an energy of ~ 1 eV for both polymers:

In evaluating equation 4, a temperature of 298 K and H_{AB} of 0.0025 eV were assumed.¹⁹

Table S4: Calculated ΔG values for the parameters above.

	$\epsilon_r = 4.0$	$\epsilon_r = 5.7$
ΔG_{solv}	-0.0199	-0.127
ΔG_{CT}	-0.212	-0.327
ΔG_{CR}	-1.380	-1.273

Table S5: Calculated ΔG values for charge recombination to the lowest triplet state rather than the ground state.

	$\epsilon_r = 4.0$	$\epsilon_r = 5.7$
ΔG_{solv}	-0.0199	-0.127
ΔG_{CT}	-0.212	-0.327
ΔG_{CR}	-0.380	-0.273

Several rate parabolas were generated with different reorganization energy values, as this parameter is not known. Low to high, these are 0.5 eV, 1.0 eV, and 1.5 eV. A value of 0.69 eV was also added, as it provided a good match to the observed effective decay rate (*vide infra*). Figure S25 shows that the resulting Marcus rate parabolas mostly predict charge recombination in the inverted region or, in the most extreme case, at the top of the parabola. Our experimental data shows the opposite trend. Charge recombination is *slower* in the samples in aqueous media, not faster. While this can clearly be seen qualitatively in the data, in Figures S39 through S45, we fit the fs-ps TA population modeling output with first-order rate constants such that it can be compared to the output of the Marcus rate equations more quantitatively.

The dry experimental data can be fit at the longest timescales (≥ 1 ns) with a rate constant of $1.9E8 s^{-1}$, while the wet films can be fit with a rate constant of $\sim 1E8 s^{-1}$. The fact that the observed recombination in the dry medium is nearly twice as fast as the in the wet films does not match the predictions from application of the Marcus equation, which predicts that the dry medium should exhibit slower decay. If recombination were to occur to the triplet state, which is predicted to have an energy of ~ 1 eV,²⁰ the dry films are predicted by Marcus kinetics to exhibit faster recombination than separation. This appears nonsensical at first glance, but note that the observed rate of charge separation generally

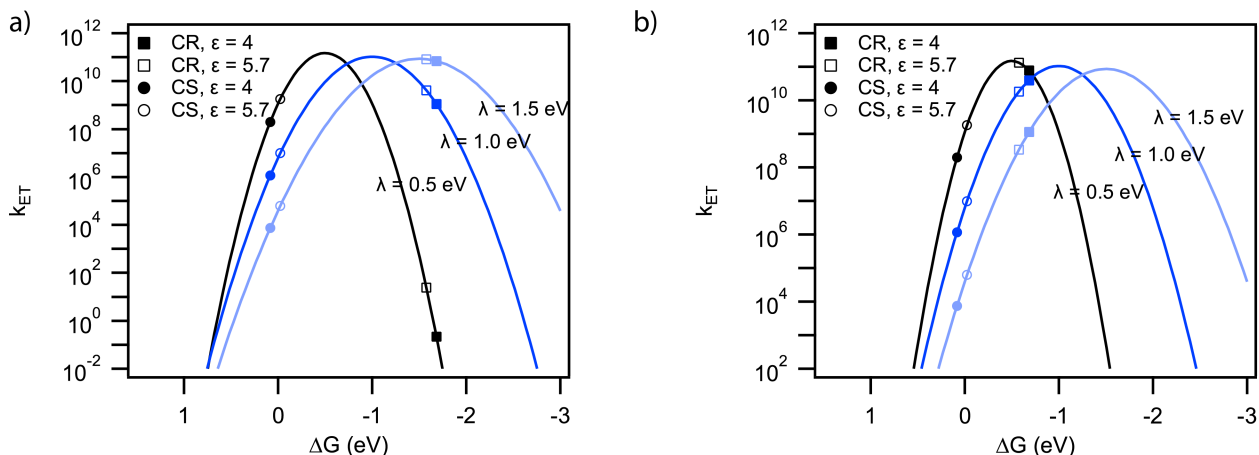


Figure S25: Calculated Marcus rate parabolas for opposite charges of 0.5 nm in a dimer separated by 1.0 nm. The calculated rates corresponding to ΔG values in media of $\epsilon_r = 4.0$ and 5.7 are indicated. Note that the curves for recombination to the ground state in (a) mostly predict CR in the inverted region, and thus the rates of CR should get faster as the charges are stabilized in the higher dielectric medium. This is the opposite of the experimental trend. (b) Recombination to the triplet state places all processes in the normal region, but predicts faster CR than CS for the dry samples.

exceeds the two-chromophore Marcus prediction by at least an order of magnitude, which can be explained by summing over the available pathways.¹⁹ While this would put the CR process in the normal region and thus predict the same trend as seen in the data, our TA and SSPIA data don't show spectral signatures corresponding to triplets. Moreover, one would need to go to quite high values of reorganization energy (> 1.5 eV) to get CR rates of the same order of magnitude as those observed in the data. Thus, while this pathway cannot be completely ruled out, it seems unlikely to be a major contributor to the observed data.

3.9 Additional Discussion of SSPIA Experiments

We note in the main text that the peak height of the samples in aqueous media is up to 43% higher than the dry film. However, the peaks also narrow substantially, reflecting a redistribution of oscillator strength rather than a simple increase or decrease of concentration, and so the peak height may not track perfectly with charge carrier density. We fit a portion of the SSPIA spectrum that appeared relatively Gaussian-shaped with a single Gaussian in the

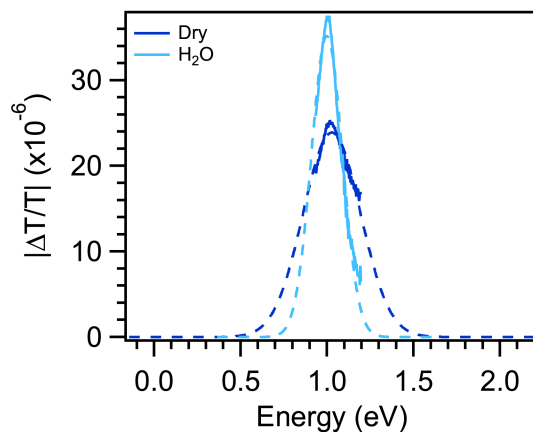


Figure S26: A comparison of the SSPIA spectra in which a relatively Gaussian portion of the spectrum was fit with a single Gaussian in an attempt to quantify peak area. The areas of the entire Gaussian in the two extreme cases are quite similar - $9.9\text{E-}6$ and $7.9\text{E-}6$ $\Delta T/T$ units, respectively.

two extreme cases - the dry film and the film that had been soaked in DI H_2O (Figure S26). The dry film peak area is $9.9\text{E-}6$ $\Delta T/T$ units and the film in dI H_2O $7.9\text{E-}6$ units, respectively. Since this single Gaussian may or may not perfectly reflect the polaron absorption spectrum, we use this to establish boundaries on the polaron yield. The yields are at least roughly the same and at best 43% greater for the films exposed to aqueous environments.

PA spectra were corrected for the phase angle φ for the modulation frequency used as retrieved from the pump scatter measurements described above. Measurements were repeated in triplicate, with each set being composed of scans from several points within the film. These were averaged together and the standard error taken. The Y channel signals, corresponding to the imaginary component of the complex signal, were scaled and flipped over the x axis for ease of comparison with the X channel signals (real part of the complex signal; see Figure S27). At 10 kHz, the shapes of the X and Y channel signals are the same within the experimental margin of error. Thus, we conclude that the part of the signal that is being lost in this frequency regime has the same spectrum as that which is not, and therefore there is only one species present.

To verify this, we undertook frequency scans at different wavelengths - the peak of the PIA

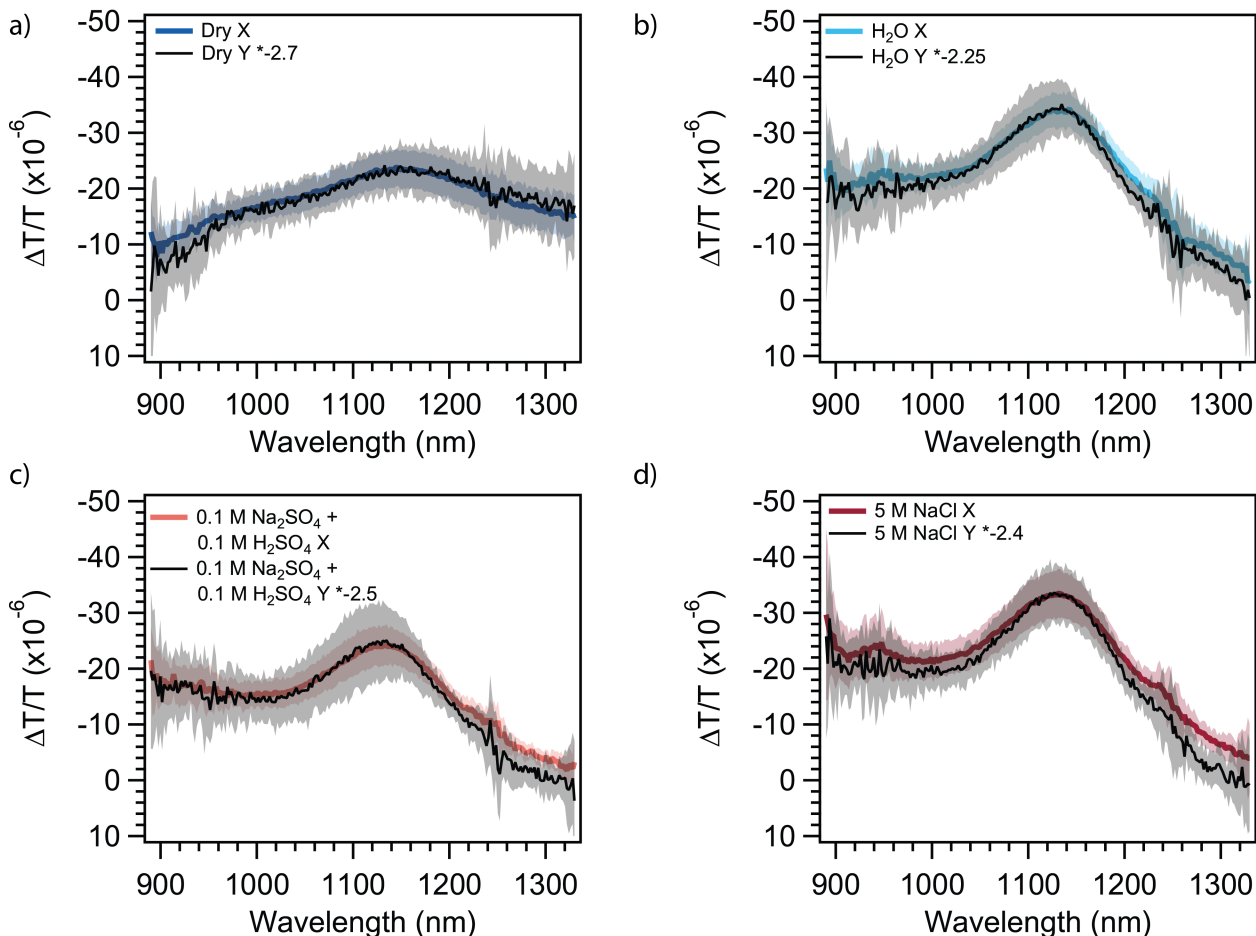


Figure S27: Photomodulation spectra of (a) the dry blend film, (b) the film in DI water, (c) the film in 0.1 M Na_2SO_4 and 0.1 M H_2SO_4 , and (d) 5 M NaCl. All spectra were taken at a modulation frequency of 10 kHz with a 640 nm CW pump laser at 1 mW. The spectra were phase-corrected using pump scatter measurements as a function of frequency as a reference. The Y channel signal has been scaled to evaluate similarity to the X channel signal.

(1130 nm in the samples in aqueous media, 1150 nm in the dry film) and 1300 nm (Figures S28 and S29). Though there was an offset between the curves at the PIA maximum and 1300 nm, all samples showed identical kinetics between the two wavelengths. Interestingly, the only curve that showed a change in signal intensity across the frequency range was the film in DI H_2O , which showed an inflection point around 250 Hz, which corresponds to a characteristic average lifetime of 637 μs .

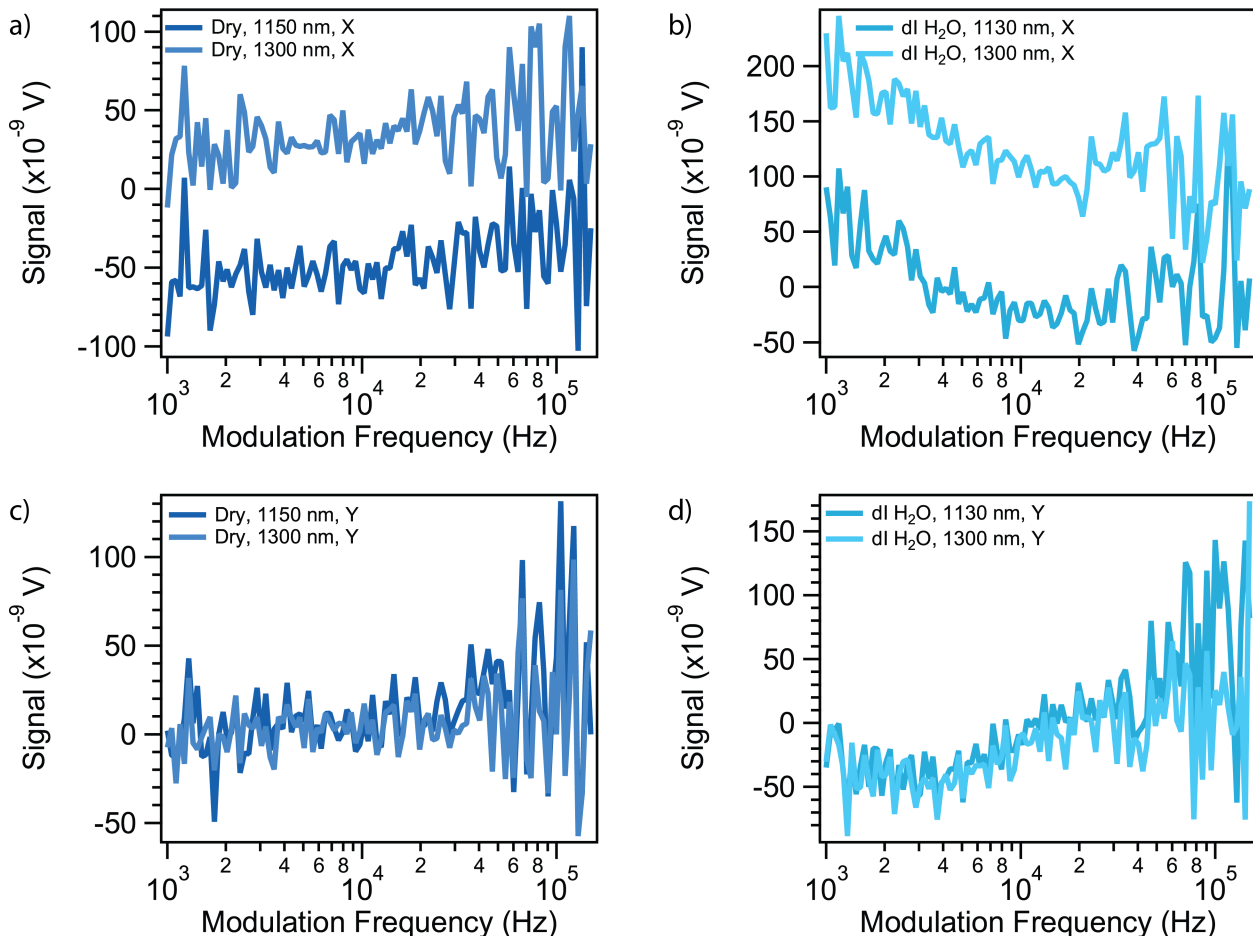


Figure S28: Frequency-dependent single-wavelength scans broken down into in-phase (X-channel) and out-of-phase (Y-channel) components of the dry film (a and c) and the film in DI H₂O (c and d). The frequency-dependent response, and therefore kinetics, at the PIA maximum and 1300 nm shoulder are identical, indicating that they arise from a single species.

3.10 Additional Discussion of the 1300 nm Photoinduced Absorption Feature in TA

To the best of our knowledge, there is one literature report that addresses a shoulder in the ΔA spectrum at 1300 nm (0.96 eV), just to the red of the positive polaron PIA, in PTB7-Th donor-acceptor blends.²⁰ Our TA spectra showed similar features in the dry films only.

Tamai *et al.* identify this as a locally-excited triplet state on the basis of thermodynam-

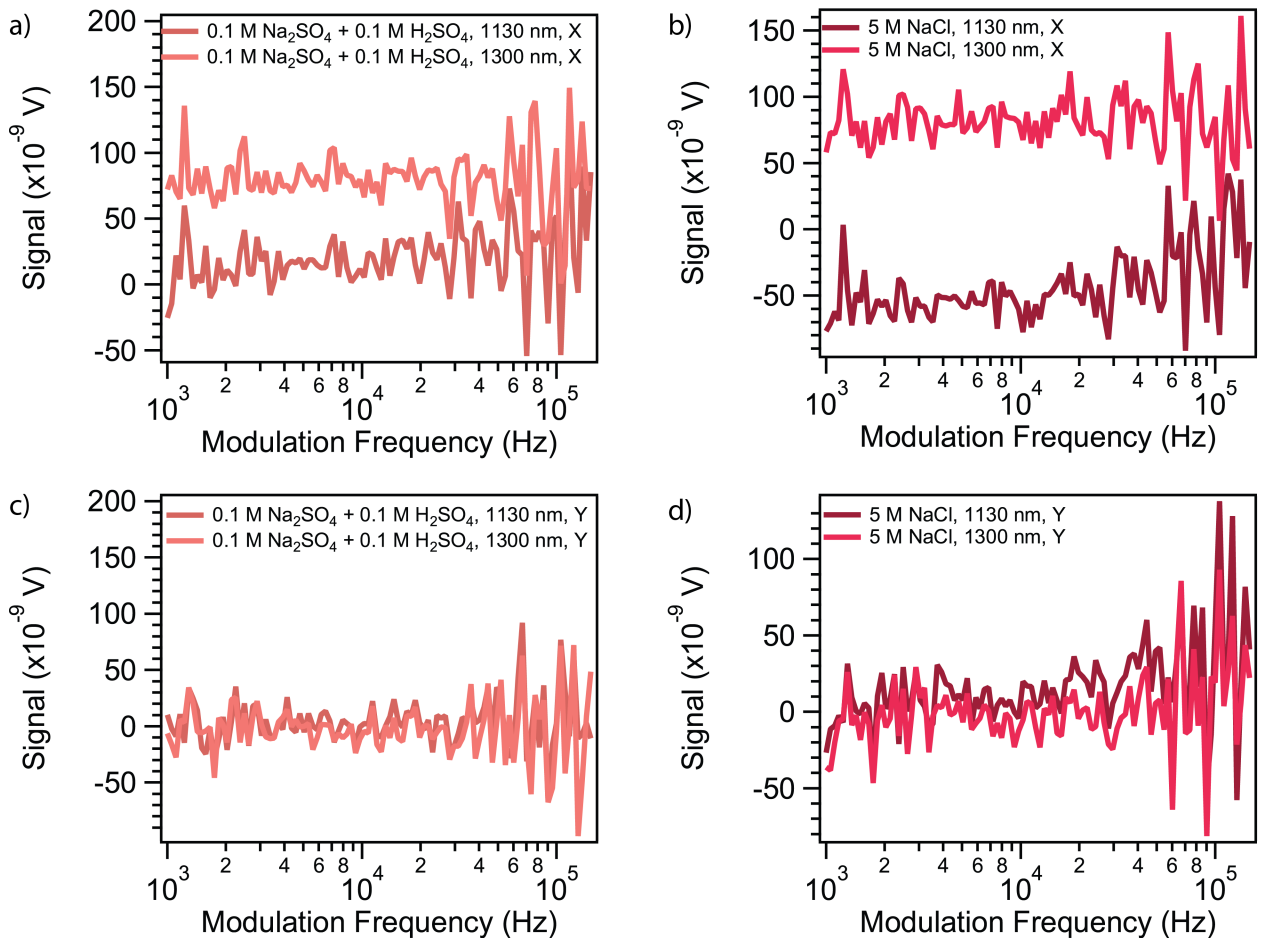


Figure S29: Frequency-dependent single-wavelength scans broken down into in-phase (X-channel) and out-of-phase (Y-channel) components of the film in 0.1 M Na_2SO_4 and 0.1 M H_2SO_4 (a and c) and the film in 5 M NaCl (c and d). The frequency-dependent response, and therefore kinetics, at the PIA maximum and 1300 nm shoulder are identical, indicating that they arise from a single species.

ics and its appearance in some blends, but not others. While this is a reasonable conclusion, the very rapid appearance (tens of picoseconds) of the feature in our films, together with its disappearance in films soaked in electrolyte, which take up a very minimal amount of water (2.3% by volume) and therefore likely experience neither a substantial change in the dielectric environment within the film nor a substantial change in the energy of the charge-separated state, led us to suggest an alternative hypothesis - that the feature could simply be the product of a different population of polarons with a different local chain structure

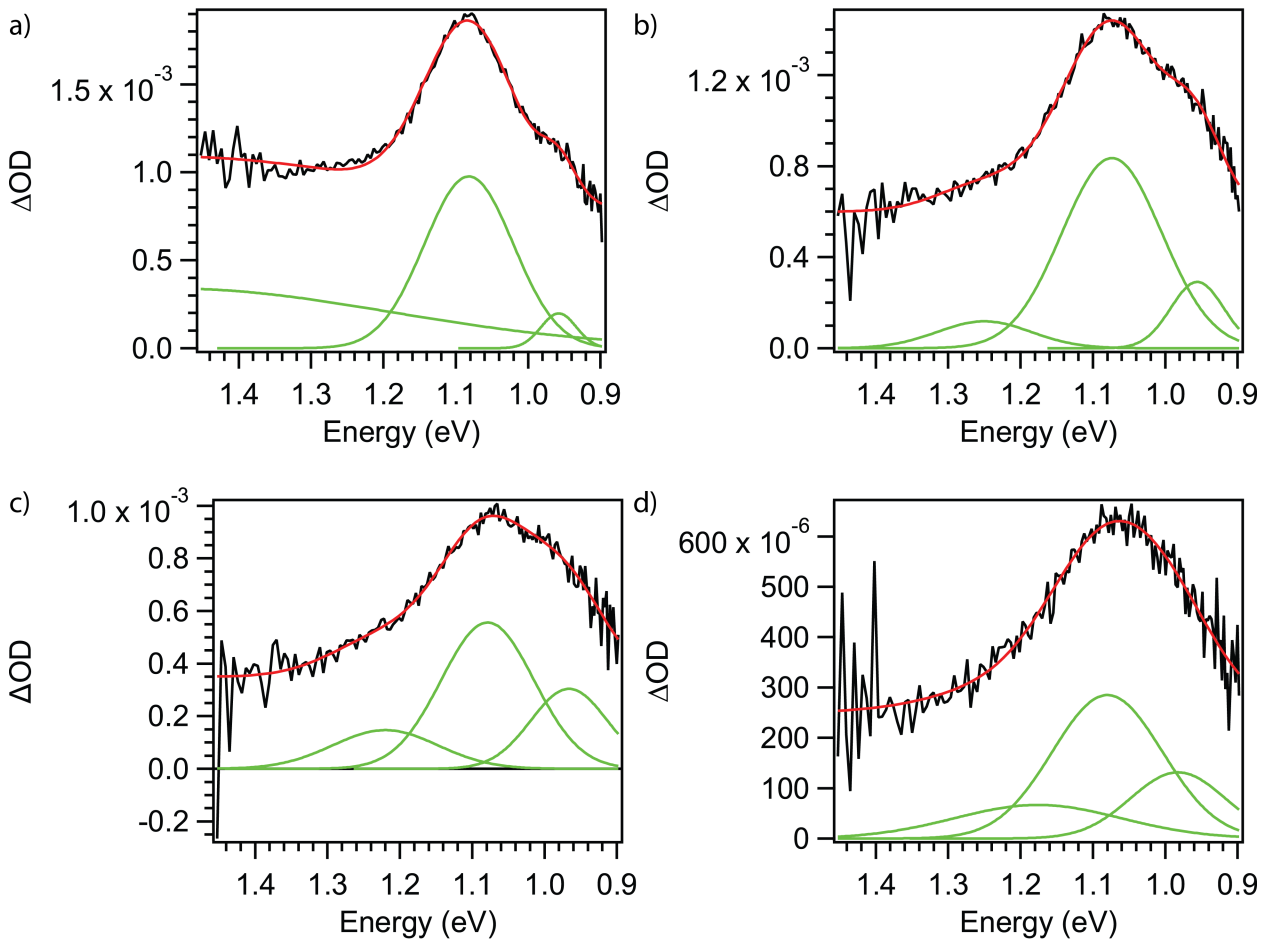


Figure S30: TA spectra of the dry film at 100 ps (a), 500 ps (b), 2000 ps (c), and 4500 ps (d) fit with a series of Gaussians. Note the Gaussian used to fit the shoulder at 0.96 eV (1300 nm).

and environment than those contributing to the main polaron peak, and that the structural changes evidenced by GIWAXS minimize the amount of this type of chain segment. Moreover, the SSPIA frequency-scan experiments (Figures S27-S29) indicate no difference in the kinetics between the PTB7-Th cation peak and the shoulder at 1300 nm, suggesting that these features arise from the same species - i.e., polarons. Still, we sought evidence for both hypotheses via triplet sensitization experiments and long-lifetime kinetic clues *via* PA.

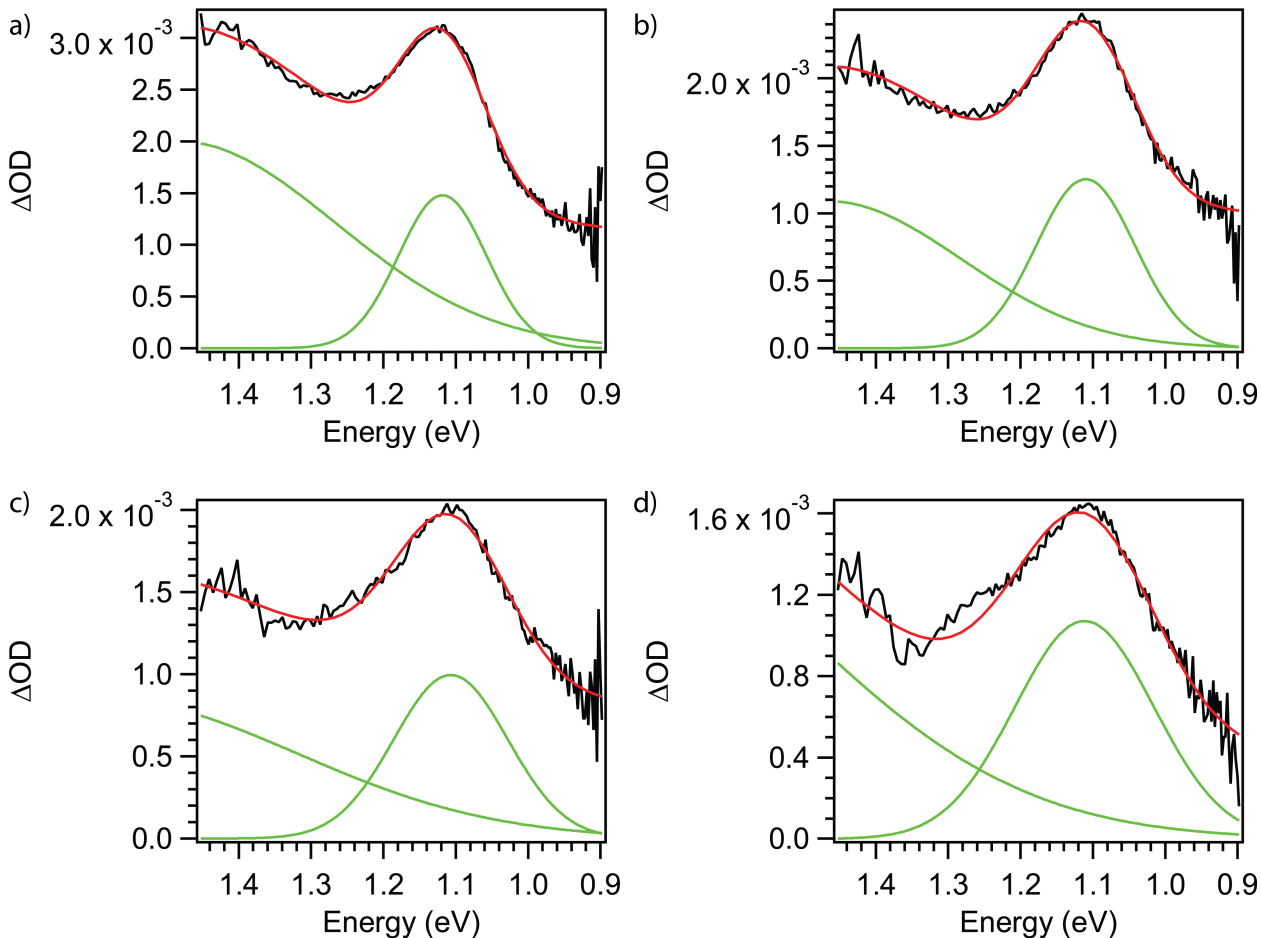


Figure S31: TA spectra of the film in dI H₂O at 100 ps (a), 500 ps (b), 2000 ps (c), and 4500 ps (d) fit with a series of Gaussians. Note that no Gaussian at 0.96 eV (1300 nm) is required to fit the data.

3.11 Computational Spectral Determination

TDDFT calculations were done on an N2200 pentamer and PTB7-Th trimer to aid in interpretation of the experimentally-obtained TA spectra. We calculated transitions from the N2200 neutral singlet and negatively-charged doublet state, as well as for the neutral PTB7-Th singlet and triplet states as well as the positively-charged doublet. A dielectric continuum of $\epsilon = 2.7$ was applied, then the calculations were repeated with a dielectric continuum of $\epsilon = 78.4$, which would correspond to fully solvating the oligomers in water.

Figure S34 shows that the P2 peak of PTB7-Th undergoes a blueshift of ~ 50 meV upon

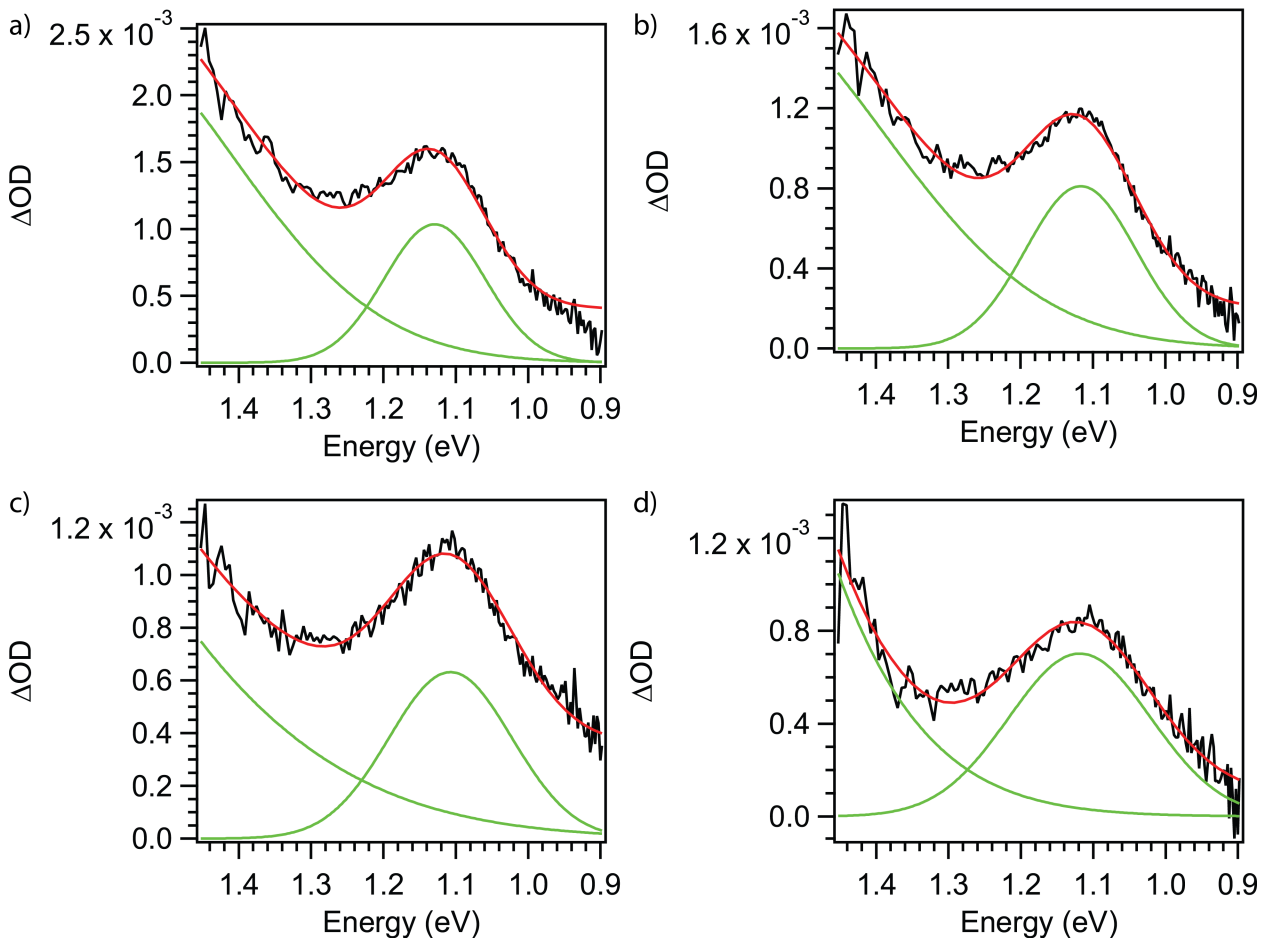


Figure S32: TA spectra of the film in 0.1 M Na_2SO_4 and 0.1 M H_2SO_4 at 100 ps (a), 500 ps (b), 2000 ps (c), and 4500 ps (d) fit with a series of Gaussians. Note that no Gaussian at 0.96 eV (1300 nm) is required to fit the data.

going from the low- to the high-dielectric environment, which matches our experimental data well. Additionally, the N2200 P1, which shows up just to the red of the PTB7-Th P2 in the low-dielectric environment, experiences an even greater blueshift of several hundred meV, moving it far past the PTB7-Th P2 peak. Thus, the shoulder observed experimentally at 1300 nm is likely the N2200 P1 peak, which then gets blueshifted so much upon exposure to electrolyte that the shoulder is no longer present.

A few important caveats are necessary here. Our FTIR (Figure S15), XRR (Figure S8), and GIWAXS data (Figure S10) all indicate that very little water is actually being

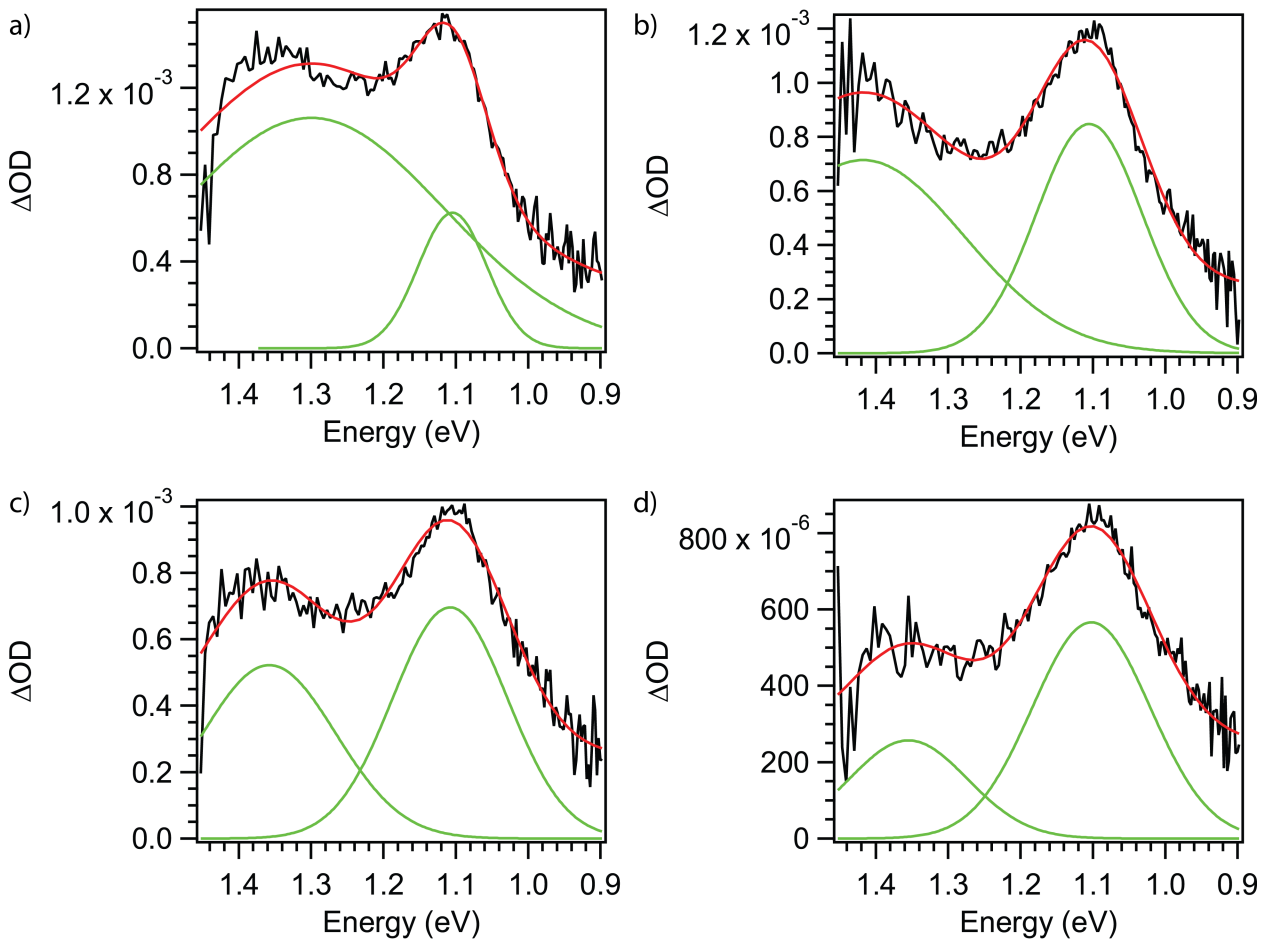


Figure S33: TA spectra of the film in 5 M NaCl at 100 ps (a), 500 ps (b), 2000 ps (c), and 4500 ps (d) fit with a series of Gaussians. Note that no Gaussian at 0.96 eV (1300 nm) is required to fit the data.

taken up into the film and that a much greater degree of structural change is occurring. These simulations are done on individual chains in a dielectric continuum of $\epsilon = 2.7$ or 78.4. The latter would correspond to a fully-solvated chain, which is clearly not the case in our experimental data. The strong evidence for morphological changes, based on GIWAXS, could have similar effects to the introduction of a strongly-polar environment - e.g., localization of the polaron. Thus, while these computational results are valuable in helping to determine the nature of the observed peaks, they cannot identify the cause of the spectral changes without further investigation to rule out possible alternatives.

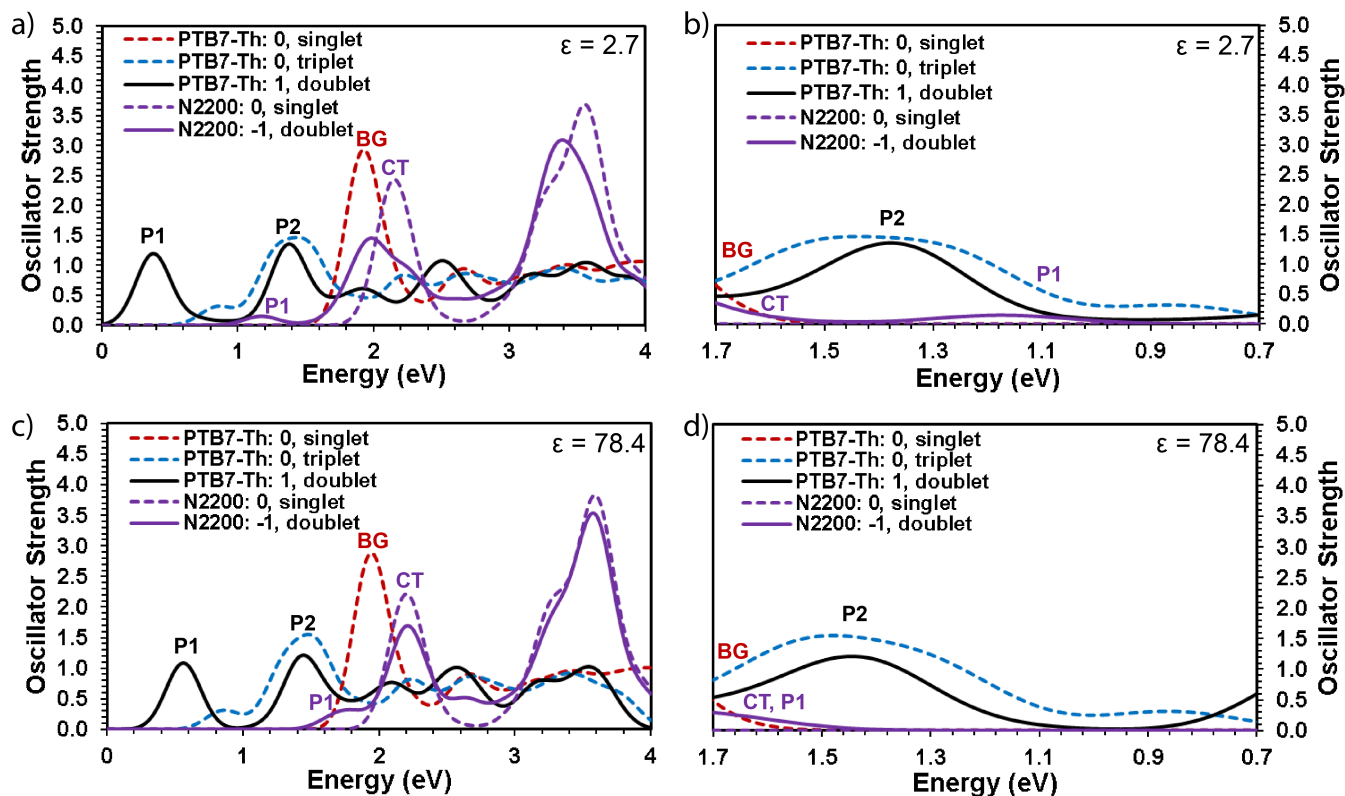


Figure S34: Computed spectra for the polymers (a and b) in a dielectric continuum of $\epsilon = 2.7$ and (c and d) $\epsilon = 78.4$. P1 and P2 correspond to the polaron-induced absorptions, BG to the band-gap of PTB7-Th, and CT to the intramolecular charge-transfer transition in N2200.

Table S6: Redox potentials of the compounds used in this study in V vs. Fc/Fc^+ .

Compound	E_{ox}^0 (V)	E_{red}^0 (V)	E_{T1} (eV)	Ref
PTB7-Th	+0.40	-1.21	1	20,21
N2200	+1.07	-0.95	1	6,22
PbPc	+0.29	-1.1	1.2	23
H ₂ TPP	+0.68	-1.61	1.4	16

3.12 Triplet Sensitization Experiments

We sought to confirm the identity of the 1300 nm shoulder using solutions containing 0.1 M PTB7-Th and 0.1 M sensitizer dissolved in toluene, with the sensitizer being either lead(II) tetrakis(4-cumylphenoxy)phthalocyanine (PbPc) or free-base tetraphenyl porphyrin (H₂TPP). Both PbPc and H₂TPP triplet energies (1.2 eV²³ and 1.4 eV,¹⁶ respectively)

Table S7: CT state energies as calculated using the formula $E_{CT} = E_{ox,D}^0 - E_{red,A}^0 - E_{T1}$.

Electron Donor	Electron Acceptor	ΔG_{CT} (eV)
PTB7-Th	PbPc	+0.30
PTB7-Th	H ₂ TPP	+0.61
N2200	PbPc	+0.97
N2200	H ₂ TPP	+1.28
PbPc	PTB7-Th	+0.30
PbPc	N2200	+0.04
H ₂ TPP	PTB7-Th	+0.49
H ₂ TPP	N2200	+0.23

should render energy transfer to the PTB7-Th triplet (reported to be around 1 eV)²⁰ thermodynamically feasible. Likewise, the reported redox potentials should render charge transfer in a nonpolar medium unfavorable. Moreover, the intersystem crossing (ISC) rates for both compounds should be much faster than the rate of diffusion of the sensitizer into the polymer chains. The reported lifetime of H₂TPP is 1.5 ms,¹⁶ which should be more than enough time to encounter polymer chains in solution. Nonetheless, no signal was observed in ns- μ s TA other than that of the sensitizer. Since the reported triplet lifetime of PbPc is rather short (50 ns),²⁴ the PTB7-Th:PbPc solution was concentrated 4x and spin-coated onto quartz in order to eliminate diffusion. Since the ISC is very rapid for PbPc,²³ it was assumed that $k_{ISC} \gg k_{CT}$ from the PTB7-Th S_1 . However, once again, no signal was observed in ns- μ s TA.

3.13 Additional Discussion of TA Data

Figure S35 shows the NIR TA spectra of PTB7-Th and N2200 films under the same excitation conditions as the blend films to show the relative contribution of each exciton to the blend film spectra (*vide infra*).

Measurements of the blend films were taken with two different thicknesses of sapphire crystal as the white-light supercontinuum (WLS_c)-generating medium and two different detectors for the visible and NIR regions of the spectrum. Additionally, measurements of the two regions were taken on different days, and variation in pump-probe overlap may have been

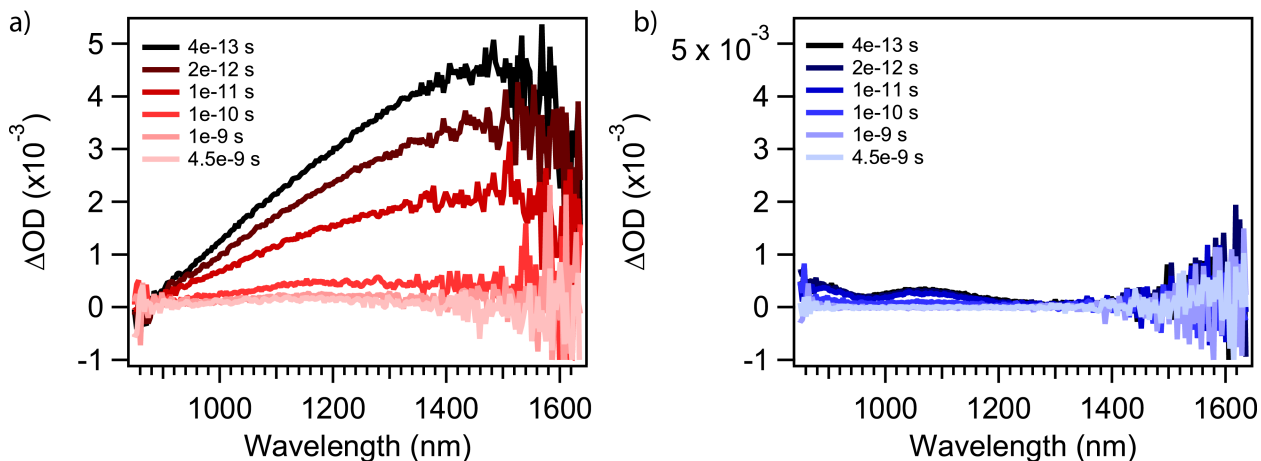


Figure S35: TA spectra of (a) neat PTB7-Th and (b) neat N2200 films. Excitation conditions were kept consistent with those of the polymer blends to illustrate the relative contributions of each polymer to the observed spectra.

present. Therefore, while the images in Figure S36 each appear as one continuous spectrum, the reader should be cautioned that they were stitched together around 835 nm and that variations in the relative intensities of the ground-state bleach (GSB) and PIAs around 900 nm, 1150 nm, 1300 nm, and 1500 nm may not be representative of actual relative differences in population.

Closer inspection of the NIR region in Figure S37 reveal several features: below 900 nm, PIA contributions from the positive polaron of PTB7-Th and negative polaron of N2200 can be seen. Note that these are higher at sub-picosecond times in the films in aqueous media than the dry one. The PTB7-Th exciton feature is the very broad PIA sloping up to a peak around 1500 nm, again as seen on sub-ps timescales. The PIA that grows in between 1100 and 1300 nm is the PTB7-Th positive polaron. Turning one's attention back to the visible in Figure S36, one should note the PIA features just to the red and blue of the GSB contain contributions from the N2200 exciton and N2200 negative polaron, though the band around ~ 440 nm appears to be especially representative of the N2200 anion.

An in-house-built global and target analysis package in Igor was used to fit the kinetics and spectra of the system at key wavelengths bands: 550-770 nm (ground-state bleach or GSB,

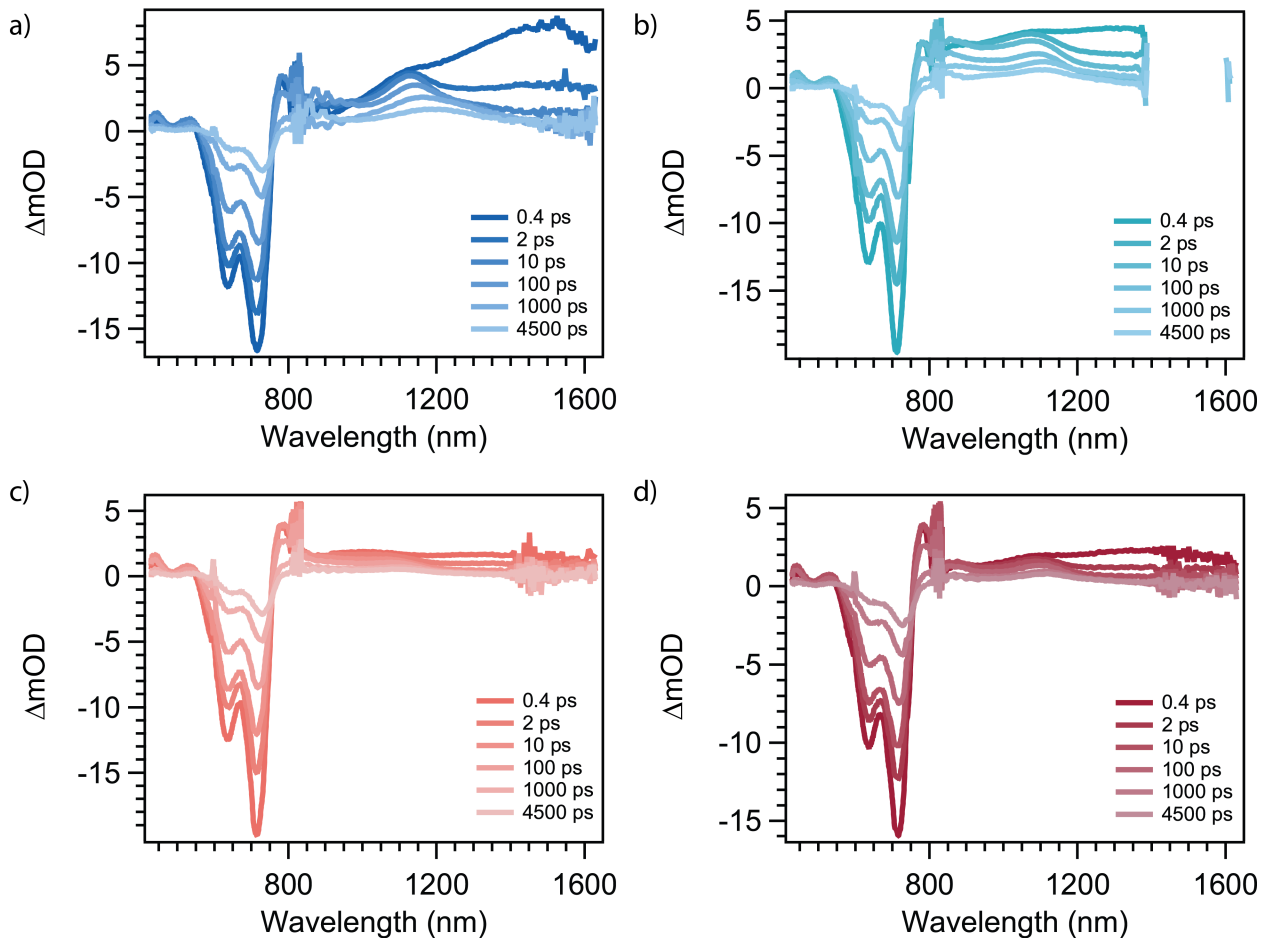


Figure S36: TA spectra of (a) the dry film, (b) the film in dI H₂O, (c) the film in 0.1 M Na₂SO₄, and (d) the film in 5 M NaCl. Due to variations in pump-probe overlap and the fact that two separate measurements were needed to collect data in the visible and NIR regions of the spectrum, one should not overinterpret relative differences in signal intensity between the ground-state bleach (\sim 700-800 nm) and PIA in the NIR.

all species contribute), 850-900 nm (polarons of both polymers),^{20,25} 1070-1150 nm (polarons in PTB7-Th with some contribution from the PTB7-Th exciton),²⁰ 1275-1325 nm (polarons in PTB7-Th with some contribution from the PTB7-Th exciton), and 1475-1525 nm (the PTB7-Th exciton; there is a small amount of signal from the PTB7-Th polaron here, however, that cannot be neglected). Whole PIA or GSB bands were averaged to account for the gradual redshifting of peaks over the course of the measurement, lest the redshift falsely show up as a population change when monitoring at a single wavelength.

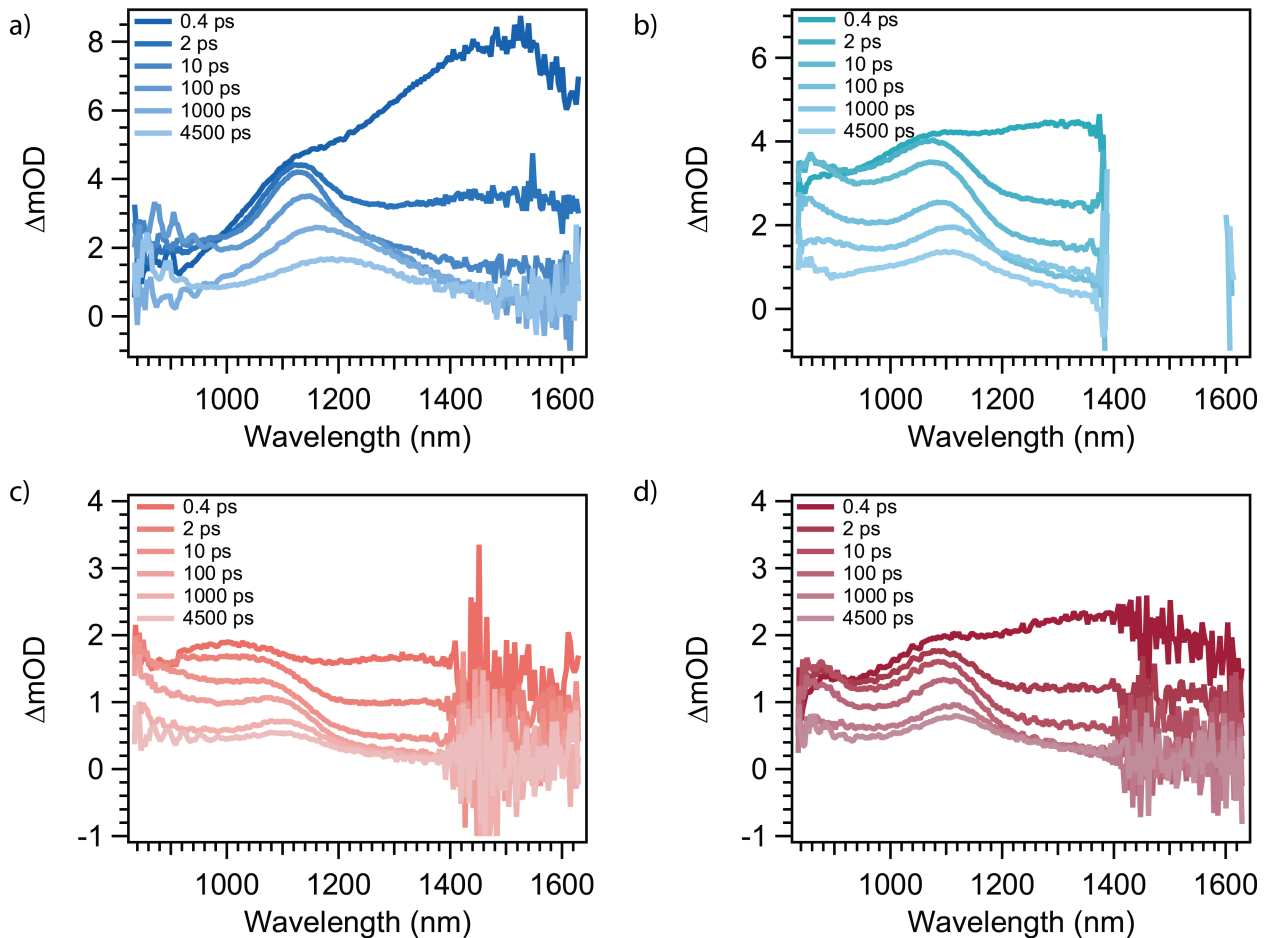


Figure S37: TA spectra of (a) the dry film, (b) the film in dI H₂O, (c) the film in 0.1 M Na₂SO₄, and (d) the film in 5 M NaCl zoomed in on the NIR. Water's strong absorption band around ~1400 nm interfered somewhat with data collection in that region in the films in aqueous media.

A kinetic model based on a numerical solution to a series of coupled differential equations was used to fit those features, and the coefficients ε_i were then fit to the population vs. time traces derived from the fits at the key wavelengths indicated previously. Some sub-IRF charge separation was apparent given the immediate appearance of signal between 800-900 nm, especially in the samples in aqueous media, so a pathway to directly populate the first charge-separated (CS) state was added in the model in addition to the exciton. Moreover, since all signals redshift over time, which is typical of a conjugated polymer system, a second CS state was added for the first CS state to empty into over time. All processes were modeled

as single-exponential decays. A purely sequential model using only the NIR portion of the spectrum was used first in order to accurately fit an effective lifetime for each state. Then, the GSB was added and used to find a decay rate to the ground state $k_{Dec} = \frac{1}{\tau_{Dec}}$, with the overall lifetime for each state fixed from the previous round such that $\frac{1}{\tau} = \frac{1}{\tau_{Dec}} + \frac{1}{\tau_{Forward}}$. $\frac{1}{\tau}$ will also be denoted k_{Eff} in the following equations. The excitation density is denoted N_0 . States were populated with a Gaussian pulse representing excitation by the pump:

$$Pulse = \frac{1}{\sqrt{2\pi}\sigma} e^{-\frac{1}{2}\left(\frac{t-t_0}{\sigma}\right)^2}$$

$$\frac{d[GS]}{dt} = -Pulse * N_0 + k_{Ex \rightarrow GS}[Ex_1] + k_{CS_1 \rightarrow GS}[CS_1] + k_{CS_2 \rightarrow GS}[CS_2]$$

$$\frac{d[Ex]}{dt} = \frac{A_1}{A_1 + A_2} Pulse * N_0 - k_{Ex \rightarrow GS}[Ex] - k_{Ex \rightarrow CS_1}[Ex]$$

$$\frac{d[CS_1]}{dt} = \frac{A_2}{A_1 + A_2} Pulse * N_0 + k_{Ex \rightarrow CS_1}[Ex_1] - k_{CS_1 \rightarrow GS}[CS_1] - k_{CS_1 \rightarrow CS_2}[CS_1]$$

$$\frac{d[CS_2]}{dt} = k_{CS_1 \rightarrow CS_2}[CS_1] - k_{CS_2 \rightarrow GS}[CS_2]$$

$$k_{Ex_{Eff}} = k_{Ex \rightarrow GS} + k_{Ex \rightarrow CS_1}$$

$$k_{CS_1_{Eff}} = k_{CS_1 \rightarrow GS} + k_{CS_1 \rightarrow CS_2}$$

Table S8: The traces used in fitting of the target analysis model and which traces were associated with which species. A 0 indicates that this wavelength range was not included in fitting the population of the associated species, while a 1 indicates that it was.

Wavelength Range (nm)	<i>GS</i>	<i>Ex</i>	<i>CS₁</i>	<i>CS₂</i>
550-770	1	0	0	0
840-900	0	0	1	1
1070-1130	0	1	1	1
1275-1325	0	1	1	1
1375-1425	0	1	1	1

Note that there could be second-order processes contributing to the decay of the excitons in addition to the intrinsic unimolecular decay, such as exciton-exciton and exciton-charge

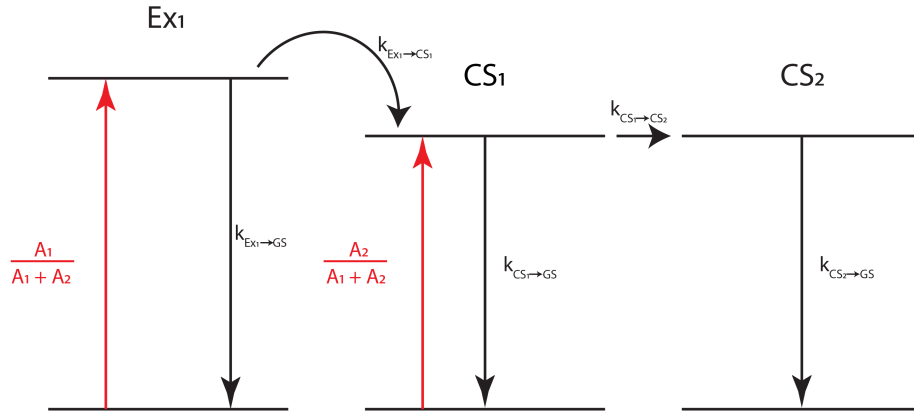


Figure S38: A schematic representation of the model used to fit the data for target analysis. The two CS states account for the spectral redshift over time. Excitation directly into the first CS state accounts for sub-IRF charge separation.

Table S9: Best-fit values for TA global fitting derived from the model for each set of conditions.

	Air	H ₂ O	0.1 M Na ₂ SO ₄ + 0.1 M H ₂ SO ₄	5 M NaCl
A_1	1	35	0.30	0.23
A_2	0	0.65	0.70	0.77
$k_{Ex \rightarrow CS_1} (s^{-1})$	5.7E11	3.9E10	2.3E10	4.0E10
$k_{Ex \rightarrow GS} (s^{-1})$	2.8E11	3.6E11	3.0E11	4.4E11
$k_{CS_1 \rightarrow CS_2} (s^{-1})$	6.8E9	4.2E9	4.1E9	4.3E9
$k_{CS_1 \rightarrow GS} (s^{-1})$	6.4E9	6.1E9	5.6E9	6.0E9
$k_{CS_2 \rightarrow GS} (s^{-1})$	1.9E8	1.0E8	1.3E8	1.1E8

annihilation. However, all samples were measured at the same fluence and had similar absorbances, so the excitation density was quite similar for all. Thus, second-order processes whose rates depend on the carrier density should be comparable for all samples measured. Moreover, in the absence of more data points (e.g., fluence-dependent measurements), a physically meaningful and unique solution for second-order rate constants was difficult to find. Regardless, the first-order rate constants employed here seem to be good approximations on the timescales for which and under the conditions for which they are employed.

The fits are generally good, with small residuals fluctuating evenly between positive and negative over the time course of the measurement. The model often struggles to match

the first few hundred fs, underestimating the Ex and the magnitude of the GSB. An extra state/process may have been able to account for this in theory, but ultimately it was omitted to avoid overfitting the data.

It should be reemphasized that in the following data, day-to-day variations in variables like pump-probe overlap may have led to varying signal strengths, even between the visible and NIR regions of the spectrum, as these had to be taken as two different measurements and stitched together. Undue emphasis should therefore not be given to heights. In fact, in some of the data, the positive and negative regions have been rescaled to allow for easier viewing of the PIA vs. GSB features.

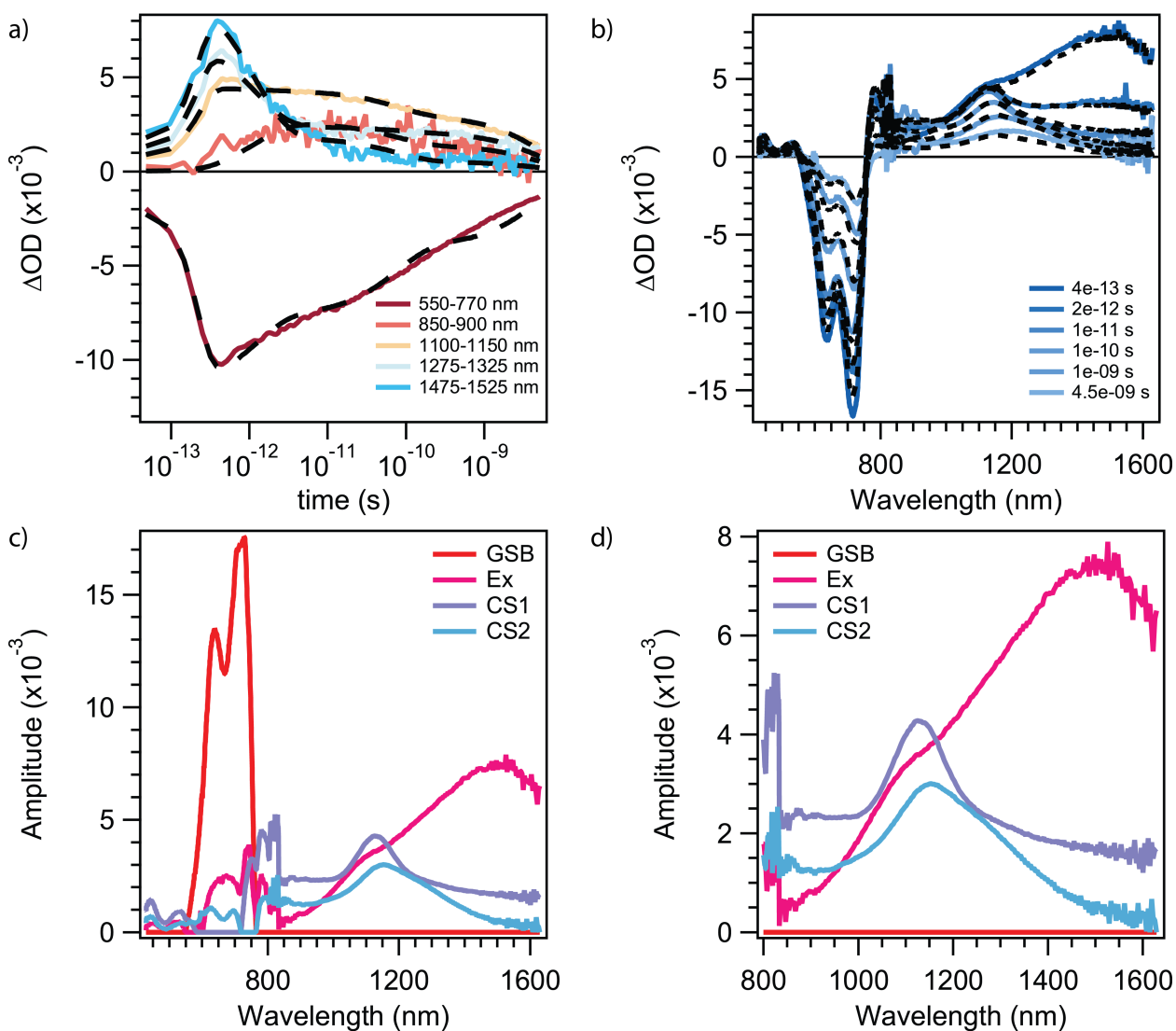


Figure S39: For the film in air, (a) kinetic fits at key wavelength ranges corresponding to important spectral features, (b) a comparison of fitted (black dashed lines) vs. experimental (blue solid lines) data, and (c and d) species-associated spectra (SAS) resulting from the population fits in (a) and the whole two-dimensional dataset.

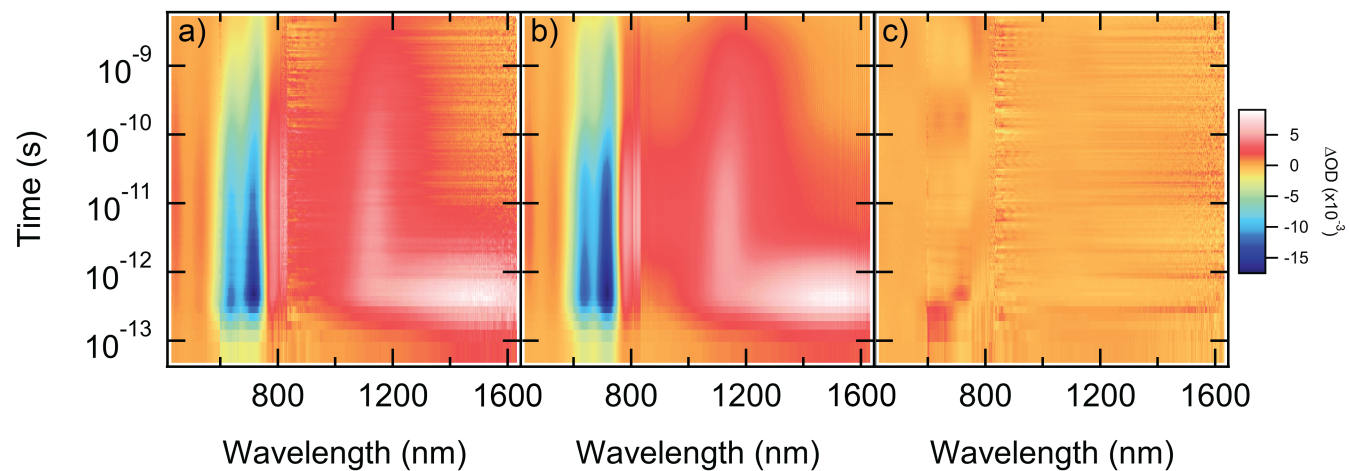


Figure S40: For the film in air, (a) the raw data as a two-dimensional map, (b) the fitted data reconstructed from the kinetic fitting and SAS, and (c) the residuals from the fitting.

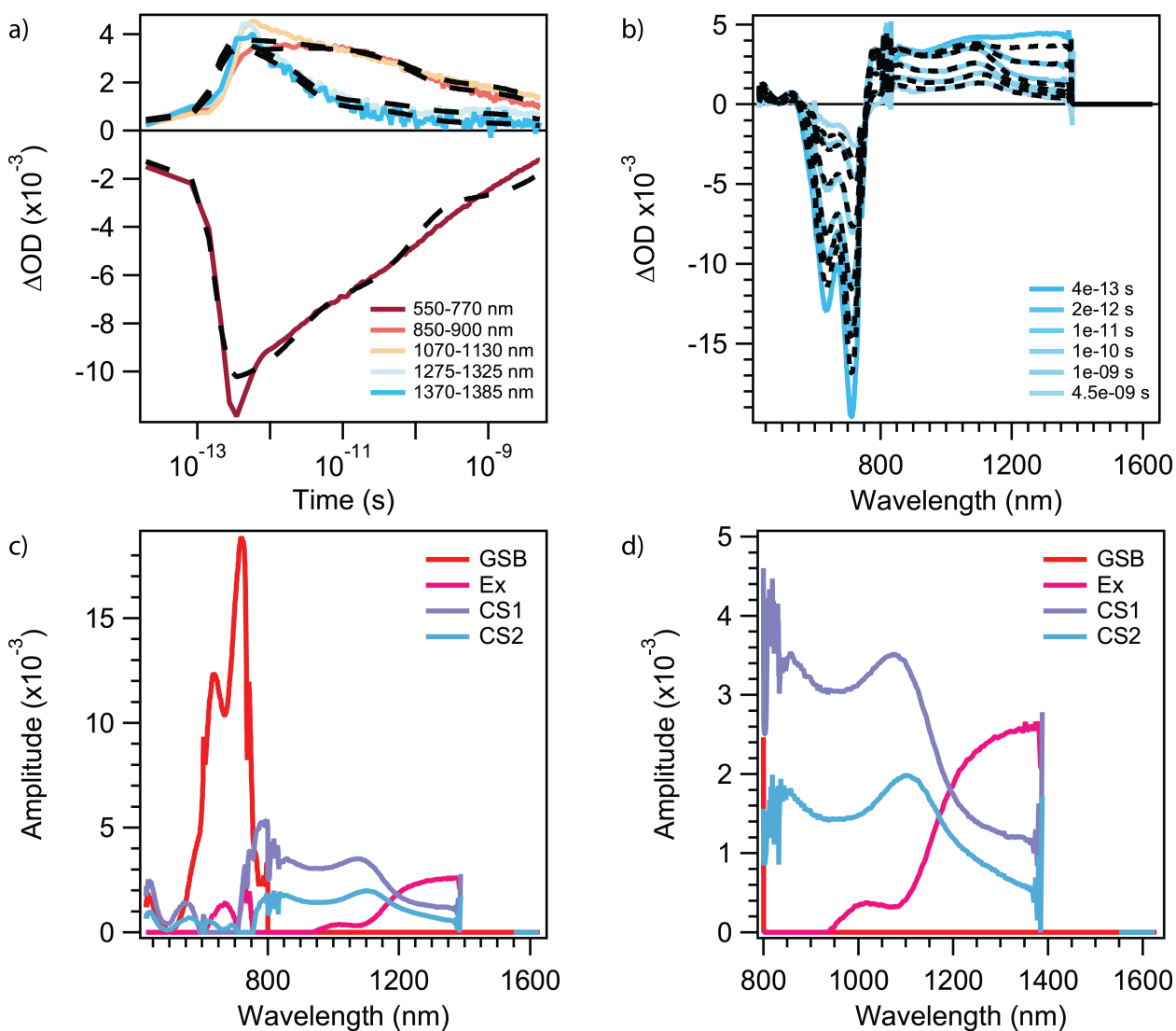


Figure S41: For the film in DI H₂O, (a) kinetic fits at key wavelength ranges corresponding to important spectral features, (b) a comparison of fitted (black dashed lines) vs. experimental (blue solid lines) data, and (c and d) species-associated spectra (SAS) resulting from the population fits in (a) and the whole two-dimensional dataset.

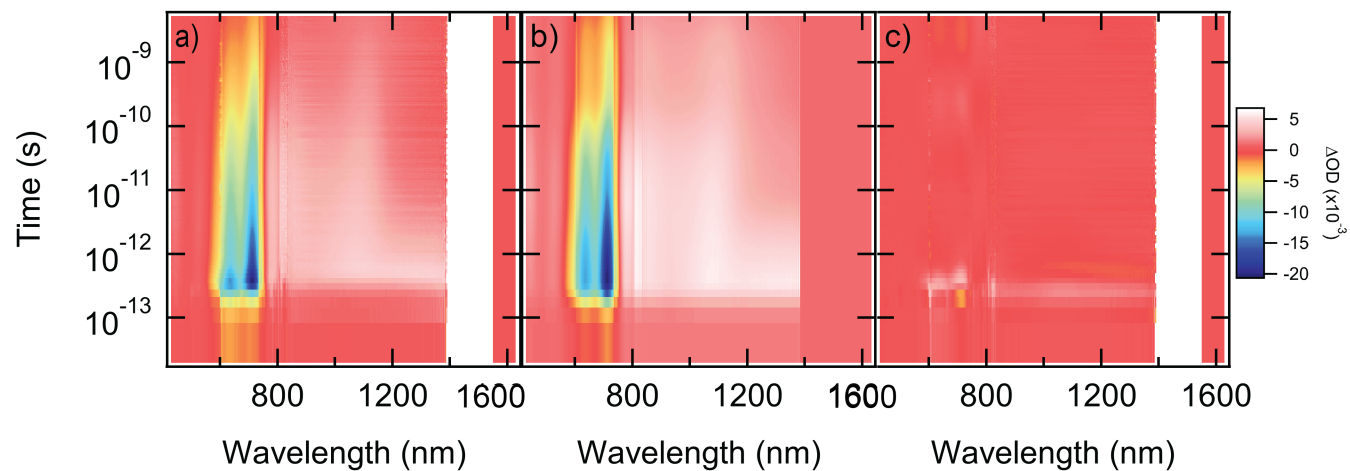


Figure S42: For the film in DI H₂O, (a) the raw data as a two-dimensional map, (b) the fitted data reconstructed from the kinetic fitting and SAS, and (c) the residuals from the fitting.

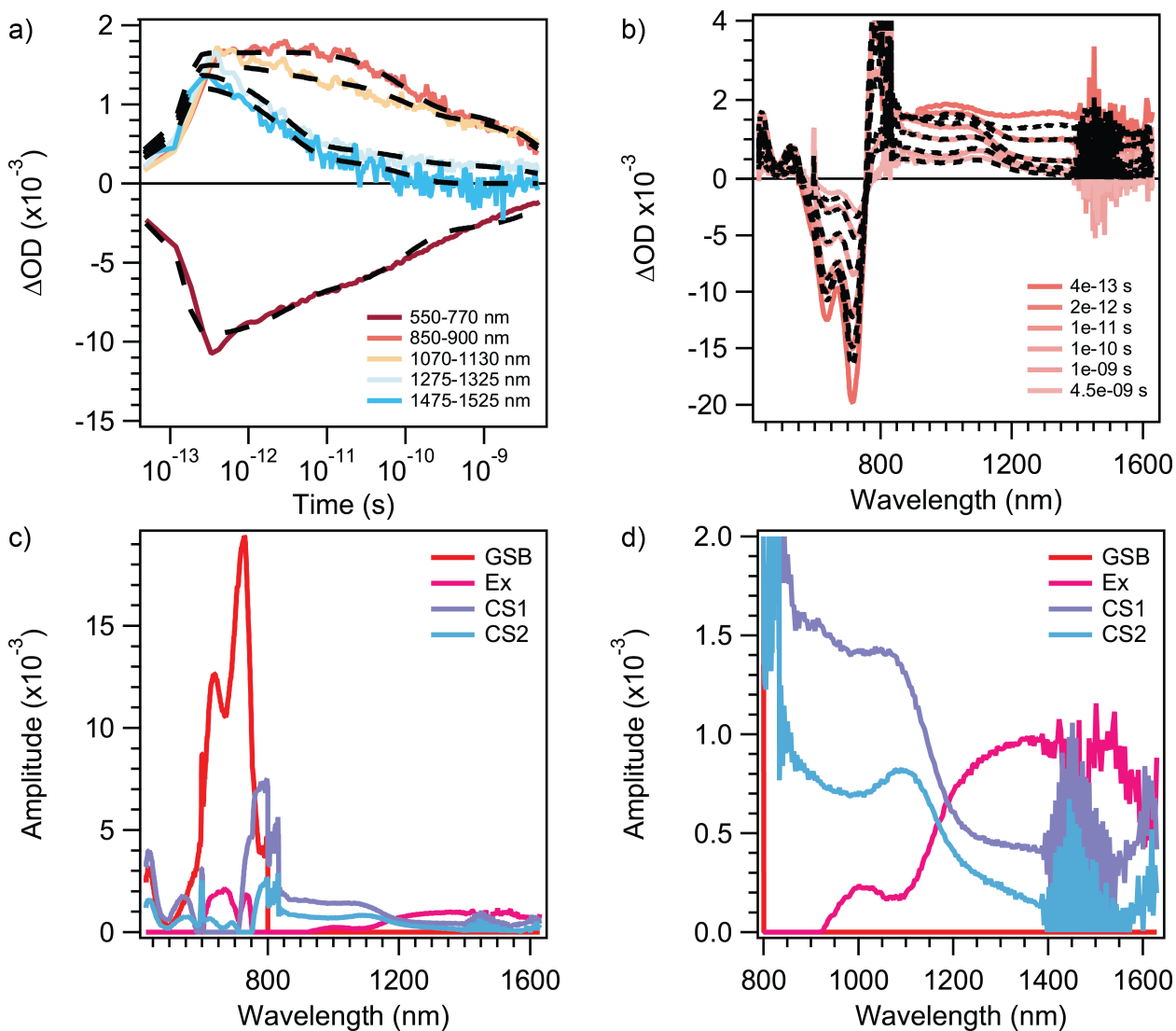


Figure S43: For the film in 0.1 M Na_2SO_4 and 0.1 M H_2SO_4 , (a) kinetic fits at key wavelength ranges corresponding to important spectral features, (b) a comparison of fitted (black dashed lines) vs. experimental (blue solid lines) data, and (c and d) species-associated spectra (SAS) resulting from the population fits in (a) and the whole two-dimensional dataset. **For (a) and (b), the positive and negative parts of the Y axis have been rescaled to facilitate easier viewing by the reader.**

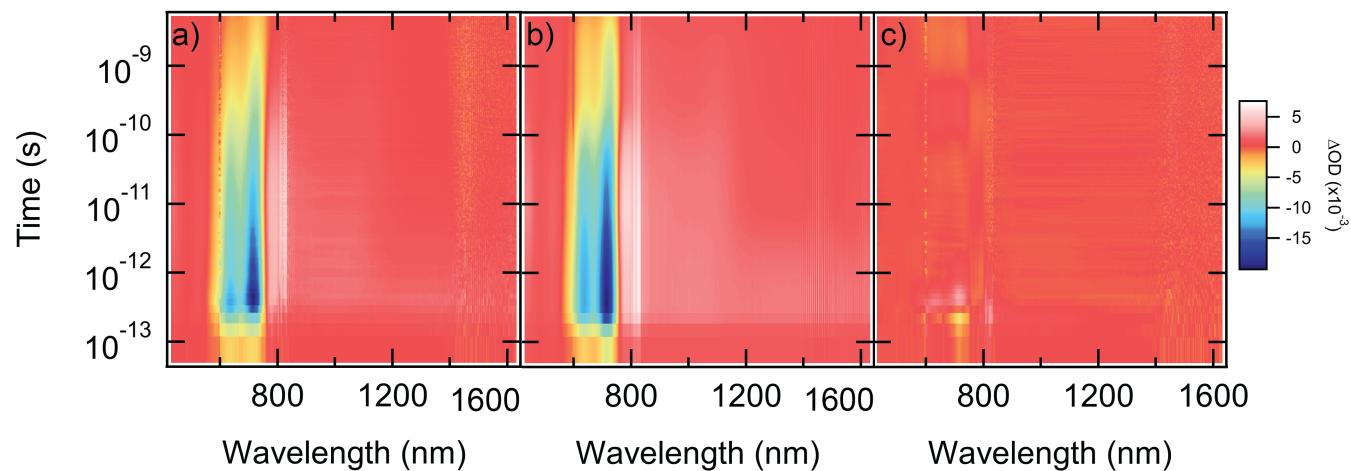


Figure S44: For the film in 0.1 M Na_2SO_4 and 0.1 M H_2SO_4 , (a) the raw data as a two-dimensional map, (b) the fitted data reconstructed from the kinetic fitting and SAS, and (c) the residuals from the fitting.

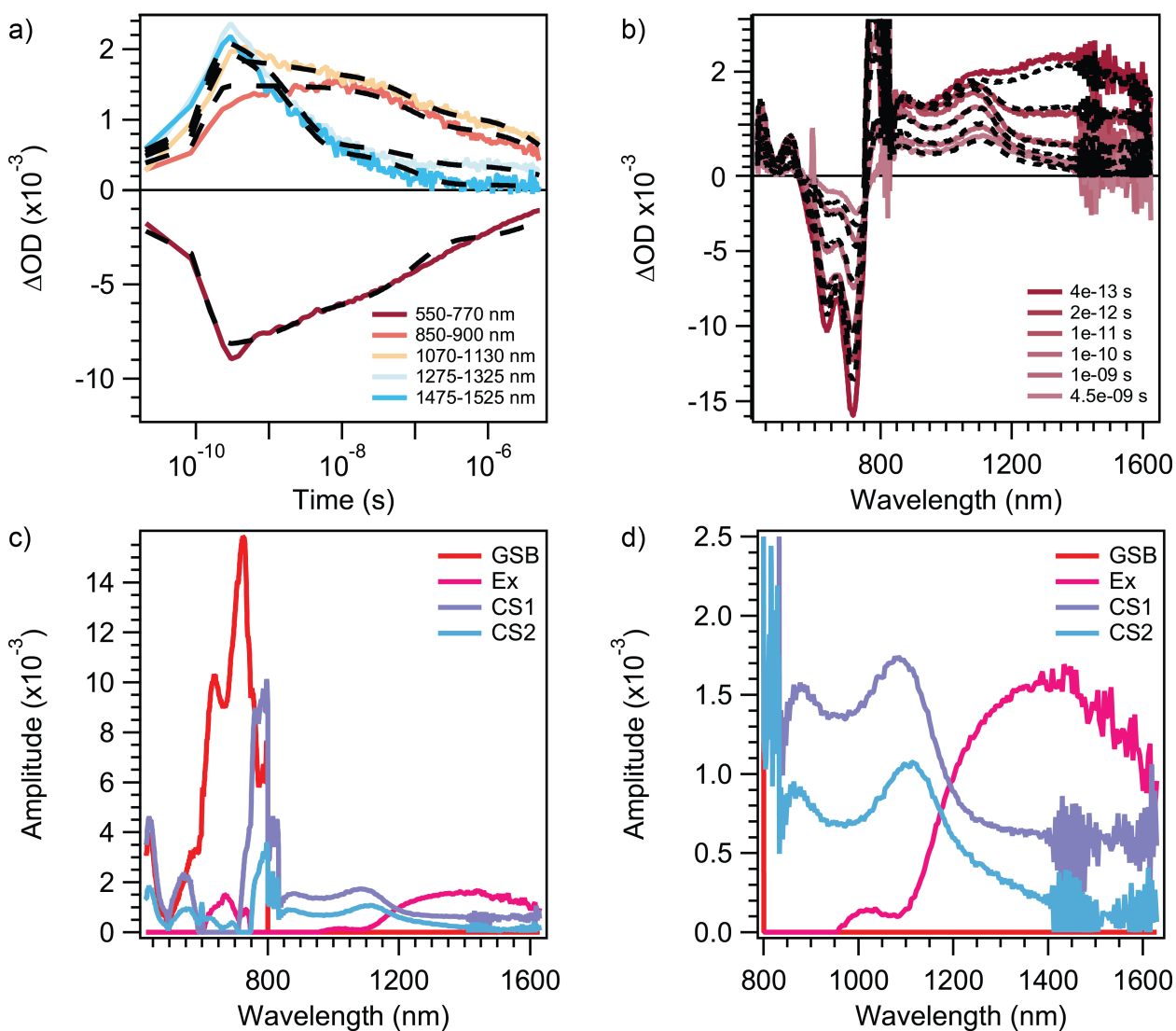


Figure S45: For the film in 5 M NaCl, (a) kinetic fits at key wavelength ranges corresponding to important spectral features, (b) a comparison of fitted (black dashed lines) vs. experimental (blue solid lines) data, and (c and d) species-associated spectra (SAS) resulting from the population fits in (a) and the whole two-dimensional dataset. **For (a) and (b), the positive and negative parts of the Y axis have been rescaled to facilitate easier viewing by the reader.**

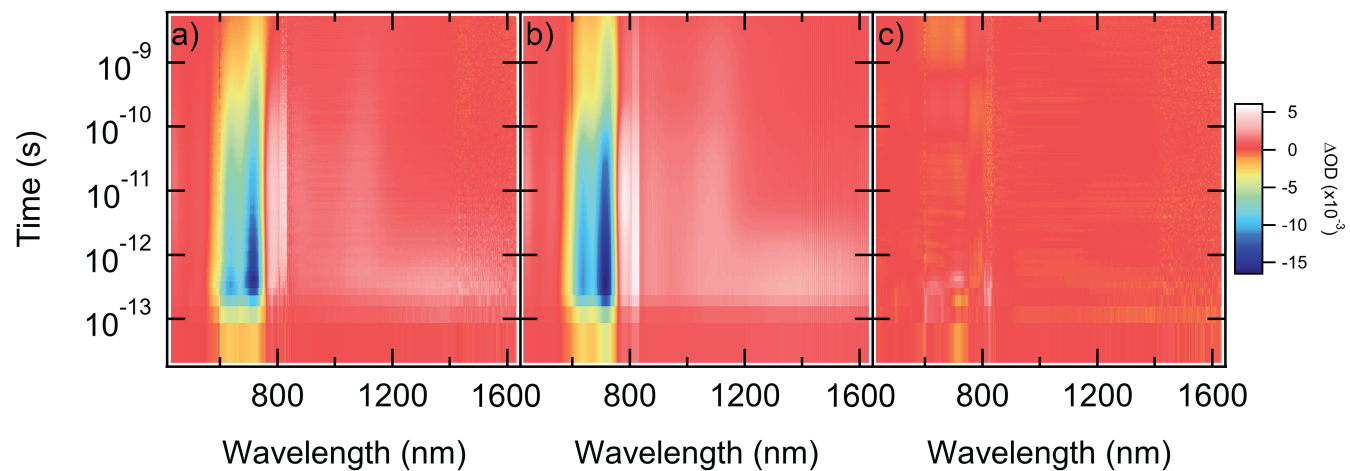


Figure S46: For the film in 5 M NaCl, (a) the raw data as a two-dimensional map, (b) the fitted data reconstructed from the kinetic fitting and SAS, and (c) the residuals from the fitting.

3.14 The Impact of Pt Nanoparticles on Charge Dynamics

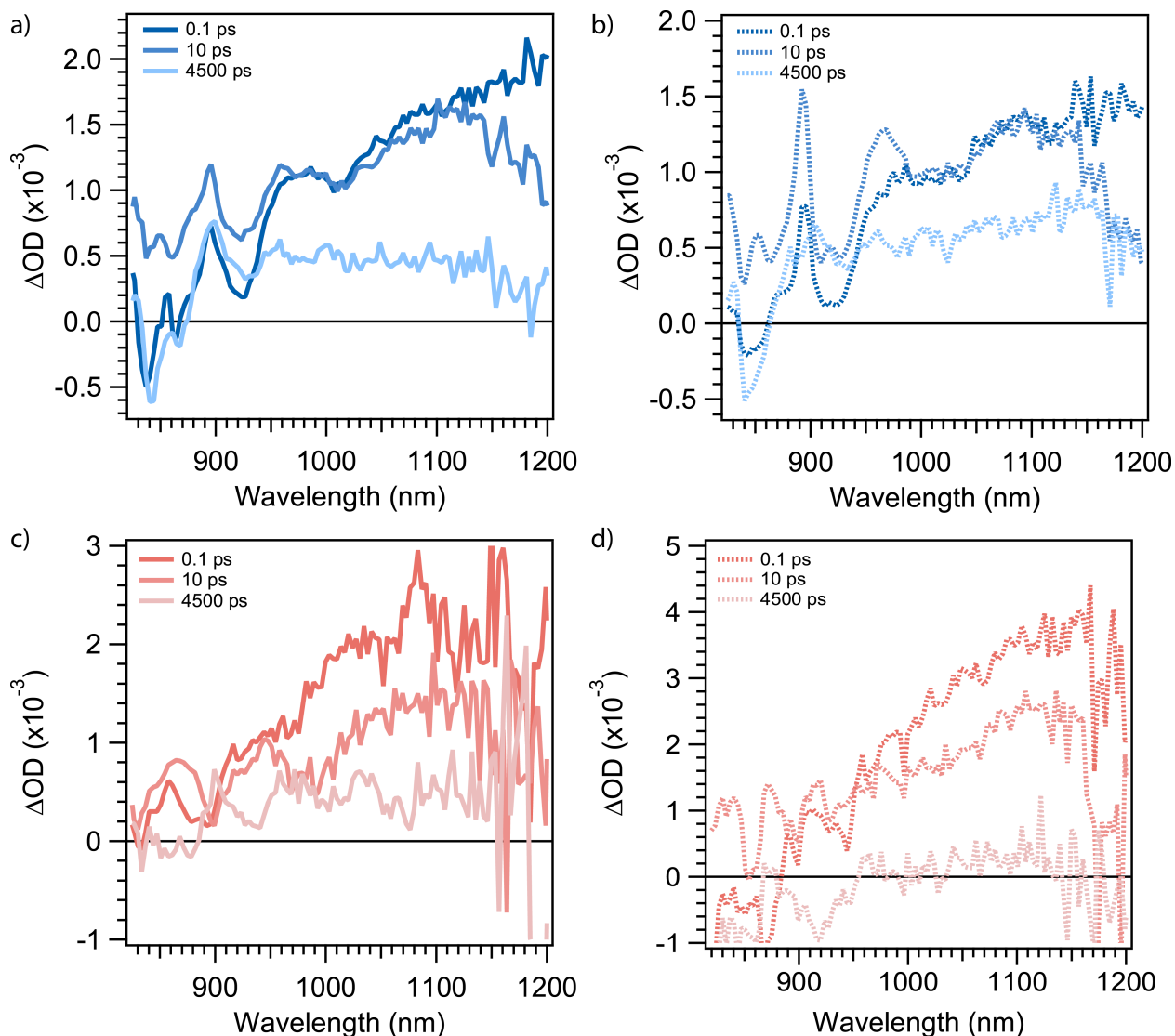


Figure S47: TA spectra of the photocathode (a) dry with no Pt nanoparticles deposited on the surface, (b) dry with Pt nanoparticles, (c) in 0.1 M Na_2SO_4 and 0.1 M H_2SO_4 with no Pt nanoparticles, and (d) in 0.1 M Na_2SO_4 and 0.1 M H_2SO_4 with Pt nanoparticles deposited on the surface.

We performed TA measurements on the photocathode with and without deposited Pt nanoparticles on the surface (Figure S47) in order to ascertain the impact of the Pt cocatalyst on the dynamics in the BHJ active layer. We used two conditions - dry and submerged in the 0.1 M Na_2SO_4 and 0.1 M H_2SO_4 electrolyte used for HER experiments. No bias was applied during these measurements. Figure S48 shows that the Pt nanoparticles have no

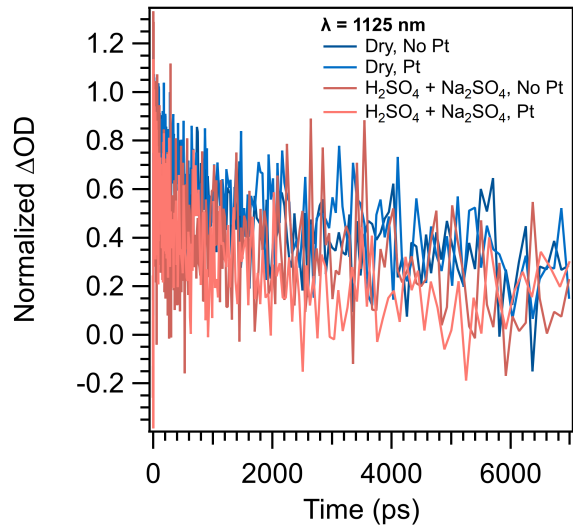


Figure S48: Kinetic traces at the PTB7-Th cation peak (1125 nm) from TA measurements of the photocathode under various conditions. Note that only the photocathode with Pt nanoparticles in 0.1 M Na_2SO_4 and 0.1 M H_2SO_4 shows differences in the observed charge carrier lifetimes.

impact on the active-layer dynamics in the dry photocathode.

References

- (1) Kosco, J.; McCulloch, I. Residual Pd Enables Photocatalytic H₂ Evolution from Conjugated Polymers. *ACS Energy Letters* **2018**, *3*, 2846–2850, Publisher: American Chemical Society.
- (2) Earley, J. D.; Zieleniewska, A.; Ripberger, H. H.; Shin, N. Y.; Lazorski, M. S.; Mast, Z. J.; Sayre, H. J.; McCusker, J. K.; Scholes, G. D.; Knowles, R. R.; Reid, O. G.; Rumbles, G. Ion-pair reorganization regulates reactivity in photoredox catalysts. *Nature Chemistry* **2022**, *14*, 746–753.
- (3) Reid, O. G.; Moore, D. T.; Li, Z.; Zhao, D.; Yan, Y.; Zhu, K.; Rumbles, G. Quantitative analysis of time-resolved microwave conductivity data. *Journal of Physics D: Applied Physics* **2017**, *50*, 493002, Publisher: IOP Publishing.
- (4) Rury, A. S.; Sension, R. J. Broadband ultrafast transient absorption of iron (III) tetraphenylporphyrin chloride in the condensed phase. *Chemical Physics* **2013**, *422*, 220–228.
- (5) Blackburn, J. L.; Zhang, H.; Myers, A. R.; Dunklin, J. R.; Coffey, D. C.; Hirsch, R. N.; Vigil-Fowler, D.; Yun, S. J.; Cho, B. W.; Lee, Y. H.; Miller, E. M.; Rumbles, G.; Reid, O. G. Measuring Photoexcited Free Charge Carriers in Mono- to Few-Layer Transition-Metal Dichalcogenides with Steady-State Microwave Conductivity. *The Journal of Physical Chemistry Letters* **2020**, *11*, 99–107, Publisher: American Chemical Society.
- (6) Wen, G.; Zou, X.; Hu, R.; Peng, J.; Chen, Z.; He, X.; Dong, G.; Zhang, W. Ground- and excited-state characteristics in photovoltaic polymer N2200. *RSC Advances* **2021**, *11*, 20191–20199, Publisher: The Royal Society of Chemistry.
- (7) Gish, M. K. et al. The Excited-State Lifetime of Poly(NDI2OD-T2) Is Intrinsically

- Short. *The Journal of Physical Chemistry C* **2024**, *128*, 6392–6400, Publisher: American Chemical Society.
- (8) Dill, R. D.; Joshi, G.; Thorley, K. J.; Anthony, J. E.; Fluegel, B.; Johnson, J. C.; Reid, O. G. Near-Infrared Absorption Features of Triplet-Pair States Assigned by Photoinduced-Absorption-Detected Magnetic Resonance. *The Journal of Physical Chemistry Letters* **2023**, *14*, 2387–2394, Publisher: American Chemical Society.
- (9) Cao, C.; Steinrück, H.-G.; Shyam, B.; Stone, K. H.; Toney, M. F. In Situ Study of Silicon Electrode Lithiation with X-ray Reflectivity. *Nano Letters* **2016**, *16*, 7394–7401, Publisher: American Chemical Society.
- (10) Soles, C.; Lee, V.; Lin, E.; Wu, W.-L. Pore Characterization in Low-k Dielectric Films Using X-Ray Reflectivity: X-Ray Porosimetry. **2004**, Publisher: Special Publication (NIST SP), National Institute of Standards and Technology, Gaithersburg, MD.
- (11) Cao, C.; Abate, I. I.; Sivonxay, E.; Shyam, B.; Jia, C.; Moritz, B.; Devereaux, T. P.; Persson, K. A.; Steinrück, H.-G.; Toney, M. F. Solid Electrolyte Interphase on Native Oxide-Terminated Silicon Anodes for Li-Ion Batteries. *Joule* **2019**, *3*, 762–781.
- (12) Ichikawa, K.; Mori, T.; Kitano, H.; Fukuda, M.; Mochizuki, A.; Tanaka, M. Fourier transform infrared study on the sorption of water to various kinds of polymer thin films. *Journal of Polymer Science Part B: Polymer Physics* **2001**, *39*, 2175–2182, Publisher: John Wiley & Sons, Ltd.
- (13) Kim, Y.; Jung, J.; Kim, S.; Chae, W.-S. Cyclic Voltammetric and Chronoamperometric Deposition of CdS. *MATERIALS TRANSACTIONS* **2013**, *54*, 1467–1472.
- (14) Rongé, J.; Nijs, D.; Kerkhofs, S.; Masschaele, K.; Martens, J. A. Chronoamperometric study of membrane electrode assembly operation in continuous flow photoelectrochemical water splitting. *Physical Chemistry Chemical Physics* **2013**, *15*, 9315–9325, Publisher: The Royal Society of Chemistry.

- (15) Savenije, T. J.; Ferguson, A. J.; Kopidakis, N.; Rumbles, G. Revealing the Dynamics of Charge Carriers in Polymer:Fullerene Blends Using Photoinduced Time-Resolved Microwave Conductivity. *The Journal of Physical Chemistry C* **2013**, *117*, 24085–24103, Publisher: American Chemical Society.
- (16) Montalti, M.; Credi, A.; Prodi, L.; Gandolfi, M. T. *Handbook of Photochemistry*, 3rd ed.; CRC Press: Boca Raton, 2006.
- (17) He, G.; Mayberry, B.; Pranav, M.; Shadabroo, M. S.; Sun, B.; Cao, Y.; Shoaee, S.; Stolterfoht, M.; Neher, D.; Lang, F. Performance-Limiting Factors in Ultralow-Bandgap PTB7-Th:COTIC-4F-Based Organic Solar Cells. *ACS Energy Letters* **2023**, *8*, 3980–3988, Publisher: American Chemical Society.
- (18) Trefz, D.; Ruff, A.; Tkachov, R.; Wieland, M.; Goll, M.; Kiriya, A.; Ludwigs, S. Electrochemical Investigations of the N-Type Semiconducting Polymer P(NDI2OD-T2) and Its Monomer: New Insights in the Reduction Behavior. *The Journal of Physical Chemistry C* **2015**, *119*, 22760–22771, Publisher: American Chemical Society.
- (19) Carr, J. M.; Allen, T. G.; Larson, B. W.; Davydenko, I. G.; Dasari, R. R.; Barlow, S.; Marder, S. R.; Reid, O. G.; Rumbles, G. Short and long-range electron transfer compete to determine free-charge yield in organic semiconductors. *Materials Horizons* **2022**, *9*, 312–324, Publisher: The Royal Society of Chemistry.
- (20) Tamai, N.; Miyasaka, H. Ultrafast Dynamics of Photochromic Systems. *Chemical Reviews* **2000**, *100*, 1875–1890.
- (21) Tang, Y.; Liu, L.; Deng, J.; Sun, P.; Yan, D.; Peng, W.; Huang, X.; Xiao, M.; Tao, Q.; Yu, D. Incorporating a weak acceptor unit into PTB7-Th to tune the open circuit voltage for non-fullerene polymer solar cells. *Tetrahedron* **2023**, *131*, 133214.
- (22) Zhou, L.; He, X.; Lau, T.-K.; Qiu, B.; Wang, T.; Lu, X.; Luszczynska, B.; Ulanski, J.; Xu, S.; Chen, G.; Yuan, J.; Zhang, Z.-G.; Li, Y.; Zou, Y. Nonhalogenated Solvent-

- Processed All-Polymer Solar Cells over 7.4% Efficiency from Quinoxaline-Based Polymers. *ACS Applied Materials & Interfaces* **2018**, *10*, 41318–41325, Publisher: American Chemical Society.
- (23) Pace, N. A.; Clikeman, T. T.; Strauss, S. H.; Boltalina, O. V.; Johnson, J. C.; Rumbles, G.; Reid, O. G. Triplet Excitons in Pentacene Are Intrinsically Difficult to Dissociate via Charge Transfer. *The Journal of Physical Chemistry C* **2020**, *124*, 26153–26164, Publisher: American Chemical Society.
- (24) Joy E. Haley; Douglas M. Krein; Weijie Su; David J. Stewart; Rachel Renkel; Thomas M. Cooper Understanding photophysics of metallated tetrakis(cumylphenoxy) phthalocyanines in epoxy and PMMA. 2020; p 112770M.
- (25) Pankow, R. M.; Harbuzaru, A.; Zheng, D.; Kerwin, B.; Forti, G.; Duplessis, I. D.; Musolino, B.; Ponce Ortiz, R.; Facchetti, A.; Marks, T. J. Oxidative-Reductive Near-Infrared Electrochromic Switching Enabled by Porous Vertically Stacked Multilayer Devices. *Journal of the American Chemical Society* **2023**, *145*, 13411–13419, Publisher: American Chemical Society.